이학석사 학위 논문

α-Mn_2O_3 nanowires coated with conductive polymer for Li-ion battery anode materials : Synthesis, characterization, and applications

리튬 이온 이차전지의 음극 물질에 사용되는 전도성 고분자로 코팅된 알파 망간 옥사이드 나노 와이어의 합성 및 응용

2016 년 2 월

서울대학교 대학원

화학부 무기화학전공

김 성 준

M. S. Dissertation

α-Mn_2O_3 nanowires coated with conductive polymer for Li-ion battery anode materials : Synthesis, characterization, and applications

Supervisor : Professor Byeong-Hyeok Sohn

Major : Inorganic Chemistry

February 2016

By Seong-Jun Kim

Department of Chemistry

The Graduate School

Seoul National University

Abstract

α-Mn_2O_3 nanowires coated with conductive polymer for Li-ion battery anode materials : Synthesis, characterization, and applications

Seong-Jun Kim

Department of Chemistry, Inorganic Chemistry

The Graduate School

Seoul National university

Transition metal oxides have been considered as promising lithium storage materials that undergo a conversion reaction with Li ion, exhibiting high specific capacity. Among them, manganese oxides have high capacity compared to other metal oxides, and also their costs are inexpensive. However, capacity fading during cycling is the most serious obstacle for their commercialization. To slove the problems, poly(3,4-ethylenedioxythiophene) polystyrene sulfonate (PEDOT:PSS) was coated onto α-Mn_2O_3 nanowires while maintaining the structure of α-Mn_2O_3. PEDOT:PSS on the α-Mn_2O_3 reduced the resistance of the sur-

face and protected the surface electron channels from the pulverization effect of the charge–discharge operation. α-Mn_2O_3/PEDOT:PSS showed excellent cyclability with a reversible capacity of 1450 mAh·g^{-1} after 200 cycles at a current density of 100 mA·g^{-1}. An increase in capacity was observed with continuous cycling, which may be attributed to further oxidation of the manganese species and a reversible reaction of the gel-like polymer on the manganese surface. The results demonstrate that PEDOT:PSS enhances the electrochemical activity by providing electron channels and prevents pulverization caused by the charge and discharge process.

Keywords : manganese oxide, PEDOT:PSS, capacity increasing, abnormal capacity, lithium ion battery

Contents

List of figures scheme and tables

Figures

Scheme

Tables

Chapter 1.

α-Mn_2O_3 nanowires coated with conductive polymer for Li-ion battery anode materials : Synthesis, Characterization, and Applications

1. Introduction

Interest on electric vehicles (EVs) and energy storage systems is continuously increasing because of the depletion of fossil fuels and increasing environmental pollution [1-2]. Thus, many researchers have investigated a variety of energy storage devices such as lithium ion batteries (LIBs) [3-5], sodium ion batteries (NIBs) [6-8], and electrochemical capacitors [9]. There are three types of mechanisms reacting with Li ion according to anode materials. (1) An intercalation reaction, in which lithium ions are inserted to/removed from the host materials during charge–discharge cycles. For example, lithium ions are inserted to/removed from between a graphite lattice [$Li^+ + C_6 + e^- \leftrightarrow LiC_6$], (2) a reaction resulting from the alloying of Li metal with metal elements such as Sn, Ge, Sb, Zn, In, Bi, and Cd (Li_xM) , and (3) a “conversion” reaction (or redox reaction). Many transition metal oxides react with lithium ions ($MO_x + 2xLi+ + 2xe^- \leftrightarrow M + xLi_2O$) [10].

Many transition metal oxides can be easily prepared with various nanoscale morphologies and structures [11-15]. Moreover, these materials can exhibit even beyond the theoretical capacity calculated based on conversion reaction mechanism [11-13, 16-28]. It is reported that it can be explained by conjugate charge storage reactions which involve

space charge layer between lithium salts and metal surface [27-28], further oxidation of Mn^{2+} to Mn^{4+} in manganese oxides [19] and reversible formation of gel-like polymer [16].

Manganese-based oxides are considered promising anode materials for LIBs due to their high specific capacity, low toxicity, and low cost, and lower operating voltage than that of other conversion reaction-based materials such as Fe-, Co-, and Ni-based oxides [29]. Manganese oxides have various phases such as MnO, Mn_3O_4, MnO_2, and Mn_2O_3 [30]. Among the various morphologies, one-dimensional (1D) manganese oxide nanostructures such as nanowires (NWs) and nanotubes (NTs) have been studied for many energy applications. 1D nanostructured materials have advantages on facilitating electrical transport, and also effectively accommodates volume expansion. Also, they have short ion diffusion pathway, which enhances rate capability [31]. However, 1D nanostructured Mn_2O_3 has been rarely investigated in spite of its high theoretical capacity (1018 $mAh \cdot g^{-1}$) and many other advantages. Because intrinsic low electric conductivity of manganese oxides reduces its electrochemical performance. Thus, many advanced studies have been carried out to overcome these intrinsic problems. For example, Ma et al. doped copper into Mn_2O_3 [32] and Liu et al. coated carbon onto MnO particles to enhance conductivity of materials [33]. Wang et

al. controlled morphology by synthesizing Mn_2O_3 nanoplates [34]. Also, Yang et al. synthesized Ag–Si core–shell nanowall arrays using Ag cores as electron-conducting pathways, which enhanced the stability and conductivity of Si anodes [35].

Herein, a new composite of Mn_2O_3 nanowires and Poly(3,4-ethylenedioxythiophene) polystyrene sulfonate (PEDOT:PSS). PEDOT:PSS is a conductive polymer mixture. The PSS part carries a negative charge due to the deprotonated sulfonyl group and the PEDOT part has conjugated rings that carry a positive charge. PEDOT:PSS has very high conductivity (ca. 300 $S \cdot cm^{-1}$) and high stability [36]. Previously research shows that PEDOT:PSS coating on the cathode material can improve electronic conductivity of the electrode and electrochemical stability [51-53]. Her at al. and Arbizzani et al. prepared cathode materials using electrosynthesis of PEDOT and Yue et al. made nano-silicon/PEDOT:PSS composites for Li ion battery anode materials, but they have complex process to obtain their products due to polymerization step [51,52,54]. PEDOT:PSS also applied to 3DOM FeF3 which reacts through a conversion reaction. The novel 3DOM/PEDOT composite was synthesized by in-situ polymerization of 3,4-Ethylenedioxythiophene (EDOT) which secured both electron and ion channels [55]. Composite of carbonaceous materials/metal oxides de-

signed to improve the conductivity is usually synthesized in too reductive condition for maintaining structure of metal oxides. However, in our composite of α-Mn_2O_3 nanowires and PEDOT:PSS, α-Mn_2O_3 nanowires maintained its structure by virtue of a mild condition for PEDOT:PSS coating process. The nanosized metal oxides particles agglomerate together to stabilize their surface energy, which lead to poorly dispersed active materials during preparing slurry, while the nanowires is well distributed within the electrode. Thus, keeping the morphology of Mn_2O_3 NWs is important to enhance the electrochemical performance for the lithium ion battery. The PEDOT:PSS coated one-dimensional manganese oxides had improved the electronic conductivity, and enhanced stability of the electrochemical active sites.

2. Experimental Section

2.1 Synthesis of α-Mn_2O_3 nanowires

The synthesis method for α-MnO_2 nanowires was similar to the reported hydrothermal method [37]. Followed by, 7.35 g of $Mn(CH_3COO)_2{\cdot}4H_2O$ (0.03 mol) was dissolved in 80 mL of deionized water in a Teflon container, followed by the addition of 6.85 g of $(NH_4)_2S_2O_8$ (0.03 mol) and 7.94 g of $(NH_4)_2SO_4$ (0.06 mol). After thorough mixing, the solution was heated in an autoclave at 140 °C for 12 h. The resulting α-MnO_2 nanowires were collected

by centrifugation and washed three times with water and ethanol. The products were calcinated at 550 °C for 1.5 h.

2.2 Coating PEDOT:PSS onto α-Mn_2O_3 nanowires

300 mg of as-prepared α-Mn_2O_3 nanowires were dispersed in a co-solvent (27 mL of water and 270 mL of ethanol) in a round-bottom flask, followed by the addition of 3 mL of PEDOT:PSS solution (CLEVIOS™ P). The mixture was sonicated for 1 h at room temperature. After sonication, we collected the black precipitate by several rinse-centrifugation cycles. The precipitate was fully dried in vacuum for characterization.

2.3 Materials characterization

$Mn(CH_3COO)_2 \cdot 4H_2O$, $(NH_4)_2S_2O_8$ and $(NH_4)_2SO_4$ were purchased from SAMCHUN. PEDOT:PSS was purchased from Clevious™. Ethanol was purchased by J.T. Baker. The morphologies of α-Mn_2O_3 nanowires and α-Mn_2O_3/PEDOT:PSS were confirmed by transmission electron microscopy (TEM, Hitachi-7600) and field emission scanning electron microscopy (FESEM, Hitachi S-4300). The crystallographic phase of α-Mn_2O_3 was identified by X-ray diffractometer (XRD, D-MAX2500-PC). The diffraction data was collected in the 2 θ range of 10˚ ~ 80˚. Energy dispersive spectroscopy (EDS) mapping of α-Mn_2O_3/PEDOT:PSS was performed by high-resolution transmission electron microscopy (HRTEM, JEM-2100F, JEOL Ltd.). Thermogravimetric analysis (TGA, SDT-Q600, TA Instruments) and Fourier trans-

form infrared spectroscopy (FT-IR, Nicolet™ iS™10, Thermo scientific) were used to characterize the amount and presence of PEDOT:PSS, respectively. The shift of binding energy was assigned by X-ray photoelectron spectroscopy (XPS, AXIS-HIS, Kratos Inc.). X-ray absorption spectroscopy (XAS) analyses were performed at the 8C beam beamline of the Pohang Light Source (PLS). The cycled electrodes for XAS analyses were prepared by disassembling of the cells, washing them with diethyl carbonate, and drying them. Finally, the electrodes were sealed with Kapton® tape. All preparation processes were carried out in an argon-filled glove box.

2.4 Electrochemical measurements

The working electrode was prepared by coating a slurry containing active material (70 wt%), Super P (as a conductive agent, 20 wt%), and polyvinylidene fluoride (PVDF, 10 wt%) onto copper foil. The coated electrodes were dried under vacuum at 120 °C for 12 h and then pressed. The electrochemical performance of the active material was examined using CR2032 button cells consisting of the as-prepared electrode, a polypropylene separator, lithium foil as the counter electrode, and 1 M $LiPF_6$ in a mixture of ethylene carbonate (EC) and ethyl carbonate (DEC) (v/v = 50:50) as the electrolyte. The cells were assembled in an argon atmosphere glove box. A WBCS3000 cycler (WonA Tech, Korea) was employed for the galvanostatic charge–discharge experiment in a voltage range of 0.01–3 V versus Li^+/Li and for cyclic voltammetry (CV) measurements from 3 to 0.01 V versus Li^+/Li at a scan rate of 0.1 $mV \cdot s^{-1}$

at room temperature. Electrochemical impedance spectroscopy (EIS) was conducted in the frequency range from 100 kHz to 0.01 Hz with an AC signal amplitude of 5 mV (Autolab, PGSTAT128N)

3. Result and discussion

3.1 Synthesis and characterization of materials

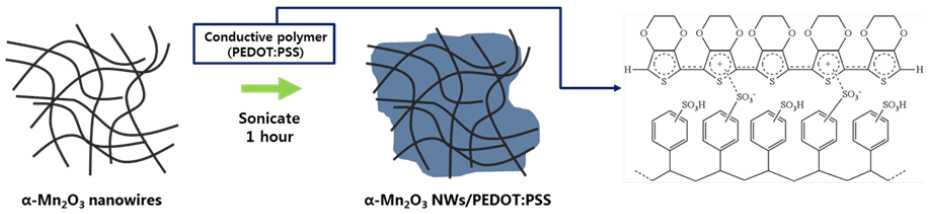

Figure 1. Schematic representation of the synthesis of α-Mn_2O_3/PEDOT:PSS.

α-MnO_2 nanowires were synthesized through a cation template-assisted hydrothermal method. These α-MnO_2 nanowires transformed into α-Mn_2O_3 at 550 °C or more in air. Fig. 1 shows the process of coating PEDOT:PSS onto the α-Mn_2O_3 nanowires. After heat treatment of as-prepared α-Mn_2O_3 nanowires at 550 °C in air, PEDOT:PSS was added to the nanowires via sonication. α-Mn_2O_3/PEDOT:PSS was obtained after 1 h in sonication. Cosolvent of DI waterand ethhanol should be used for this process. α-Mn_2O_3 nanowires have good dispersibility in ethanol but they don't in water because most hydroxyl groups on surface were eliminated during calcination. Howev-

er, PEDOT:PSS cannot disperse in ethanol but in water. So, Mn_2O_3 nanowires and PEDOT:PSS need proper ratio of two solvent. Therefore, the ratio 9 : 1 (ethanol : water, v/v) was identified as ideal ratio from dispersibility test. (**Fig. 2**)

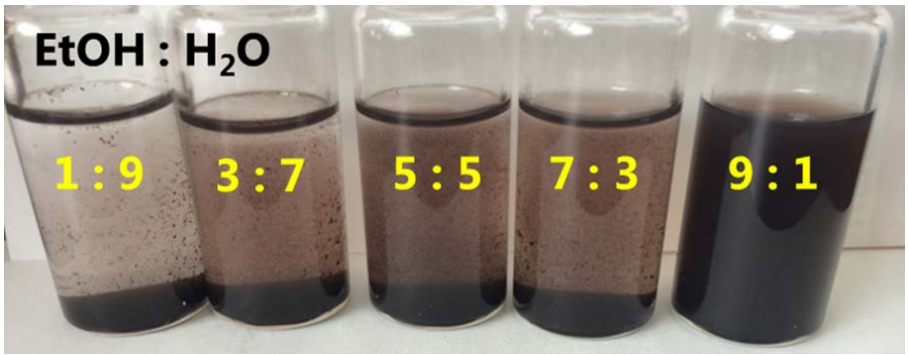

Figure 2. Dispersibility of α-Mn_2O_3 nanowires according as Ethanol/H_2O ratio.

The morphology of bare α-Mn_2O_3 nanowires are shown in TEM and SEM images (Fig. 3a-c). The prepared α-MnO_2 nanowires have 1D nanostructure with a diameter of 20 nm. The obtained α-Mn_2O_3 nanowires after heat treatment at 550 ℃ (or higher temperature) maintained their morphology even though the structures are changed. Furthermore, the morphology of α-Mn_2O_3 was still maintained after the coating process. Unlike a carbon-coating process, the PEDOT:PSS-coating process can omit heat treatment at high temperature, which

causes morphology change with a phase transition. The mild conditions of the PEDOT:PSS coating process has a significant advantage for applying conductive coatings onto electric materials.

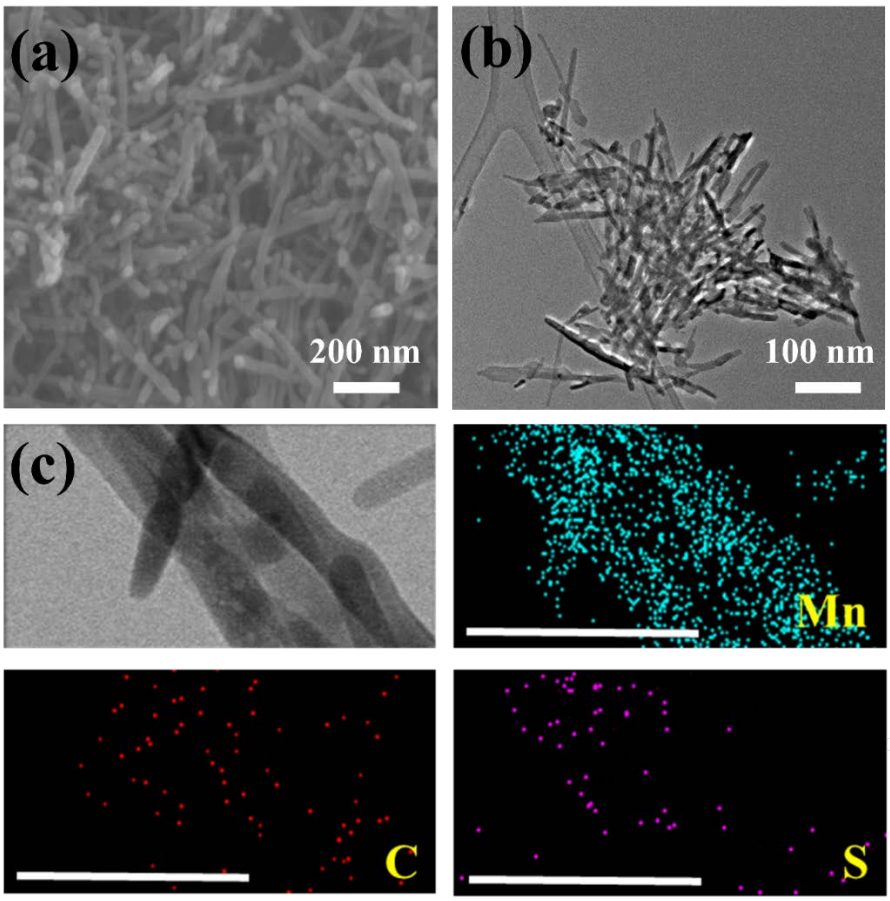

Figure 3. (a) FE-SEM and (b) TEM image of bare α-Mn_2O_3 nanowires. (c) TEM image (first picture) and EDS-mapping of bare α-Mn_2O_3 nanowires (scale bar is 200 nm)

The existence of PEDOT:PSS was characterized after the coating process by SEM, TEM, and EDS mapping (Fig. 4a-c) It is clearly seen that the diameter of α-Mn_2O_3/PEDOT:PSS nanowires is thicker than that of α-Mn_2O_3 nanowires (Fig. 4a). In addition, the coating of PEDOT:PSS on α-Mn_2O_3 nanowires is observed in TEM and EDS mapping (Fig. 4b and c). The XRD patterns of α-MnO_2 and the α-Mn_2O_3 nanowires were well matched with α-MnO_2 phase (PDF#44-0141) and α-Mn_2O_3 phase (PDF#24-508), respectively (Fig. 4d)

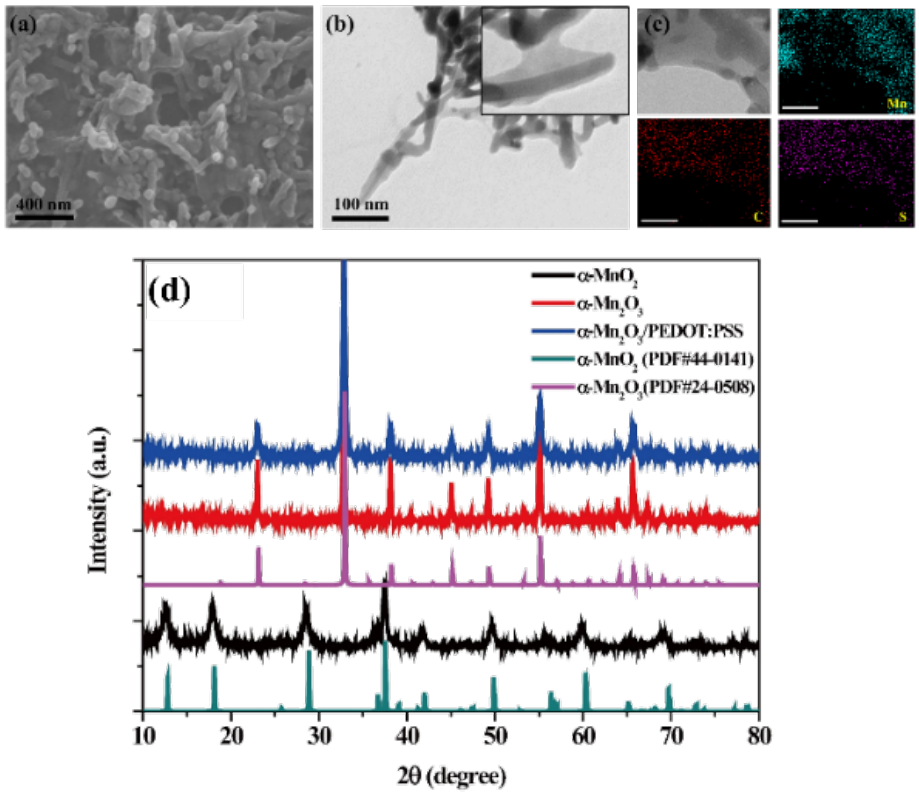

Figure 4. (a) FE-SEM and (b) TEM image of α-Mn_2O_3/PEDOT:PSS (c) EDS-mapping of α-Mn_2O_3/PEDOT:PSS (d) XRD patterns of α-MnO_2, bare α-Mn_2O_3 and α-Mn_2O_3/PEDOT:PSS.

According to TGA, approximately 23 % PEDOT:PSS was contained in α-Mn_2O_3/PEDOT:PSS nanowires (Fig. 5a). Also, the weight of bare α-Mn_2O_3 decreased because of its phase transition from α-Mn_2O_3 to Mn_3O_4, the removal of water from the surface hydroxyls, and the de-composition of a slight amount of SO_4^{2-} species on the surface [38]. The surface chemical species of α-Mn_2O_3/PEDOT:PSS and bare α-Mn_2O_3 were verified by FT-IR. α-Mn_2O_3/PEDOT:PSS exhibited unique peaks of PEDOT:PSS from 3500 to 3000 cm^{-1} and from 1700 to 750 cm^{-1} (Fig. 5b) [39]. Peaks indicating SO_4^{2-} anions (1260 to 900 cm^{-1}) and –OH groups from the adsorbed water and surface hydroxyls (~3400 and ~1600 cm^{-1}) were also found [40]. Both spectra showed peaks corresponding to the vibration of the Mn-O bond in Mn_2O_3 [41].

We further analyzed the chemical and oxidation states on surface of both materials by XPS. Binding energy shifts to lower appeared in both Mn 2p and O 1s spectra after coating (Fig. 5c and d, respectively). In addition, Messmer et al. reported that the electrostatic contribution affects binding energies [42]. The electrostatic interaction reduced the

binding energies of the Mn-O bond in the α-Mn_2O_3 nanowires. After addition of PEDOT:PSS, the two peaks of Mn 2p shifted to lower binding energy about 0.4 eV (642.4 → 642.0 eV and 654.4 → 654.0 eV, respectively) and the peaks of O 1s shifted 0.4 and 0.1 eV (530.8 → 530.4 eV and 532.2 → 532.1 eV), respectively. These O 1s peaks were caused by the presence of the S-O bond in the SO_4^{2-} anion and the adsorbed water on the surface [43].

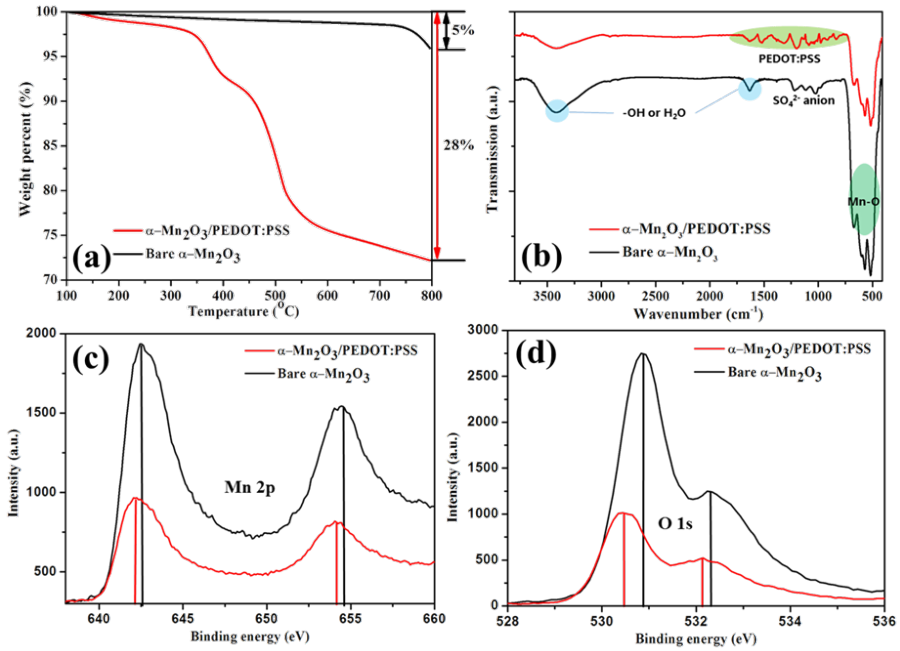

Figure 5. (a) TG analysis before and after treatment of PEDOT:PSS. (10 ℃ /min, Air condition) (b) FT-IR spectra before and after treatment of PEDOT:PSS. XPS spectras of the (c) Mn and (d) O atoms in materials before and after treatment of PEDOT:PSS.

Polythiophene group of PEDOT has positive charge that may help to attach on surface of α-Mn_2O_3 nanowires because surface charge of α-Mn_2O_3 nanowires is negative charge. (Fig 6) Two materials were attached by electrostatic interaction. Besides, sulfate anions on the surface interacted with PEDOT:PSS and they also help to stick between them.

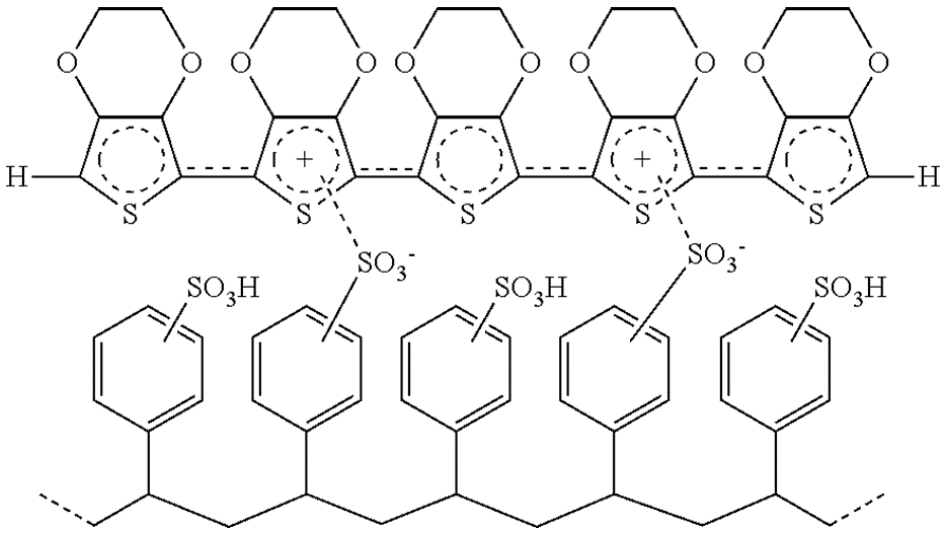

Figure 6. Illustration of PEDOT:PSS structure.

The surface potential of bare α-Mn_2O_3 nanowires is approximately -38.6 mV. After adding PEDOT:PSS, their surface charge shifts positive a little about -10.5 mV. (Table 1) PEDOT:PSS could lower the surface charge of bare α-Mn_2O_3 nanowires.

	Bare α-Mn_2O_3 NWs	α-Mn_2O_3 NW/PEDOT:PSS
1st	-41.0 mV	-9.99 mV
2nd	-37.5 mV	-11.0 mV
3rd	-37.4 mV	-10.6 mV
Average	**-38.6 mV**	**-10.5 mV**

Table 1. Zeta potential of bare α-Mn_2O_3 nanowires and α-Mn_2O_3/PEDOT:PSS.

3.2 Electrochemical performance in Li ion battery

The electrochemical performance was evaluated by galvanostatic charge and discharge measurements. Fig. 7a shows the cycle performance of α-Mn_2O_3/PEDOT:PSS and α-Mn_2O_3 at current density of 100 $mA \cdot g^{-1}$ in a potential range between 0.01 and 3 V. The specific capacities of α-Mn_2O_3/PEDOT:PSS and α-Mn_2O_3 decreased during initial several cycles [23]. However, the capacity of α-Mn_2O_3/PEDOT:PSS gradually increased after 25 cycles. The capacity reached a maximum value of 1450 $mAh \cdot g^{-1}$ after 200 cycles, whereas the capacity of α-Mn_2O_3 still under 400 $mAh \cdot g^{-1}$ after 200 cycles even though the capacity continuously increases after about 40 cycles. At higher current density, fluctuation on cycle performance was also observed. The capacity of α-Mn_2O_3/PEDOT:PSS decreased up to the 50th cycle and then started to rebound at 500 $mA \cdot g^{-1}$. These abnormal trends of increasing capacity after decreasing were further investigated through charge-discharge voltage profiles. Fig. 7c and d show the charge and discharge curves of α-Mn_2O_3/PEDOT:PSS and α-Mn_2O_3, respectively. Both α-Mn_2O_3/PEDOT:PSS and α-Mn_2O_3 show the typical lithiation and delithiation profiles of manga-

nese oxide. The first lithiation curves can be explained by dividing it into three distinct regions [44]. The first region was caused by the insertion of lithium ions into Mn_2O_3 to form $LiMn_2O_3$, followed by the diffusion of oxygen and lithium ions out of $LiMn_2O_3$ to form MnO, resulting in two quasi-plateaus above 0.3 V. The second region is an extended plateau near 0.3 V, resulting in the largest charge. The second region is related to the transformation from MnO into Mn metal and Li_2O. Finally, the third region is a sloping voltage below 0.3 V, which can be explained by interfacial insertion (or space charges). In the subsequent delithiation process, the oxidation of metallic manganese to MnO (not to Mn_2O_3) and the diffusion of lithium ions out of Li_2O occurred, which resulted in a plateau near 1.25 V. In the second lithiation process, the extended plateau near 0.3 V corresponding to the reduction of MnO to Mn^0 shifted to 0.45 V. This indicated that the obstacle of second lithiation is lower than that of the first lithiation as a result of formation of nanoscale metal cluster (<5 nm) imbedded in Li_2O matrix during the first lithiation [19]. In the lithiation curves of α-Mn_2O_3/PEDOT:PSS, main reaction occurs at plateau (0.45 V), which is related to the transformation of MnO to Mn up to 50 cycles. After 50 cycles, however, the plateau near 0.45 V gradually disappears, whereas the slope below 0.45 V gradually expands. It seems that the reaction in end of lithiation (below 0.45 V) is related to formation of gel-like polymer which is caused by pulverized nano-metal particles [16]. EIS analysis was introduced to investigate the effect of the PEDOT:PSS coating (Fig. 7e). The proposed equivalent circuits are a simplification of the real situation based on

several assumptions [45,46]. Although the α-Mn_2O_3/PEDOT:PSS electrode did not perfectly agree with the assumptions, the experimental values were consistent with the calculated data. Fig. 7e shows the Nyquist plots of α-Mn_2O_3 after 50 cycles and α-Mn_2O_3/PEDOT:PSS after 50 and 100 cycles. The equivalent circuits is presented in Fig. 7e, where R_o indicates ohmic resistance and R_f and C_f indicate the resistance of the SEI film and the capacity of the surface-passivating layer, respectively. The resistance of the charge transfer reaction and the capacitance of the double layer are represented by R_c and C_c, respectively. The values of R_o and R_f for α-Mn_2O_3/PEDOT:PSS (1.02 and 24.77 Ω, respectively) after 50 cycles were lower than the those of α-Mn_2O_3 (2.25 and 84.56 Ω, respectively). Furthermore, R_o and R_f of α-Mn_2O_3/PEDOT:PSS after 100 cycles displays lower values. This improvement is due to the coating of conductive PEDOT:PSS onto the α-Mn_2O_3 nanowire surface, which provided electron channel and served as a favorable binder agent for electrochemical microstructure reconstruction. However, the R_c value of α-Mn_2O_3 (29.78 Ω) is slightly increased after the coating (38.23 Ω for α-Mn_2O_3/PEDOT:PSS). As shown in Fig. 7f, rate performance of α-Mn_2O_3/PEDOT:PSS nanowires is also higher than that of α-Mn_2O_3 nanowires.

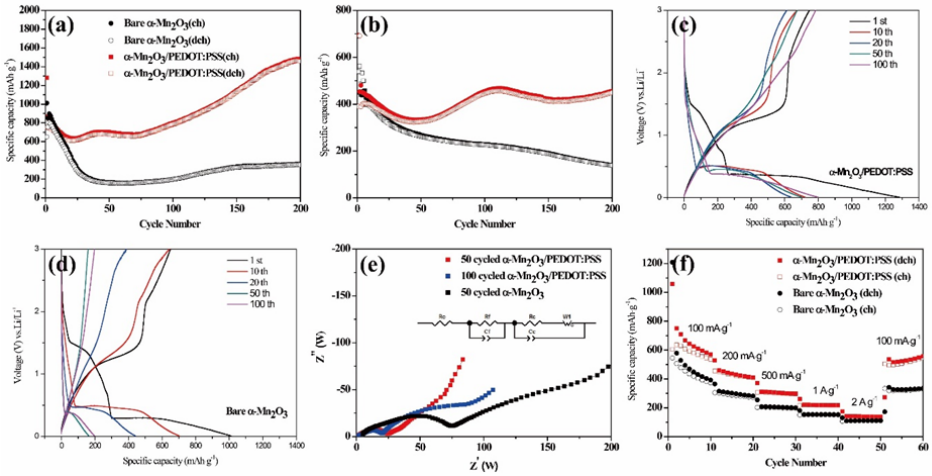

Figure 7. Cycle performances of bare α-Mn_2O_3 and α-Mn_2O_3/PEDOT:PSS at a current density of (a) 100 mA·g^{-1} and (b) 500 mA·g^{-1}. Voltage profiles of (c) α-Mn_2O_3/PEDOT:PSS and (d) α-Mn_2O_3. (e) AC impedance of α-Mn_2O_3/PEDOT:PSS and α-Mn_2O_3 with equivalent circuit. (f) Rate properties of α-Mn_2O_3/PEDOT:PSS.

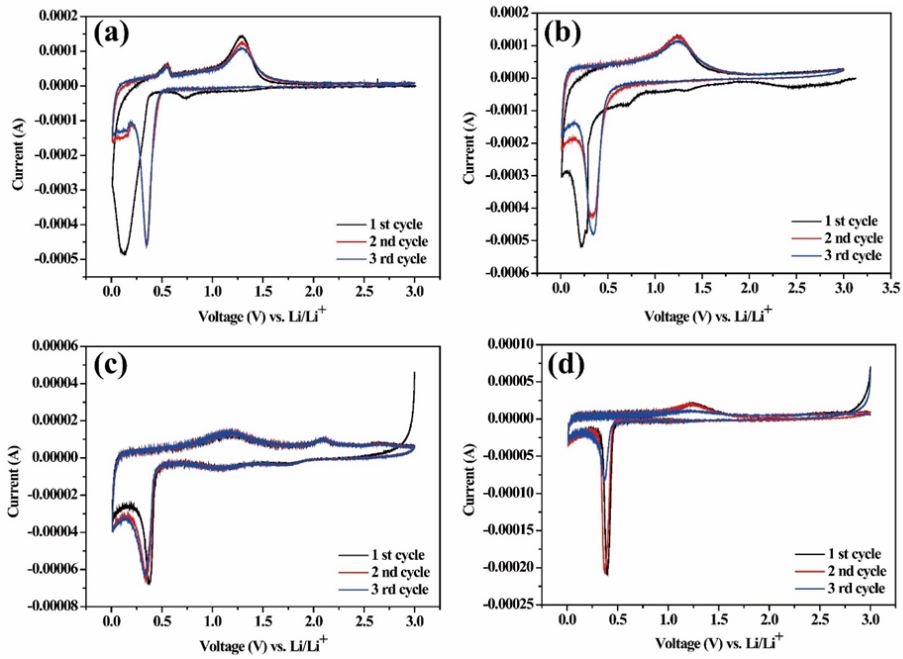

Figure 8. Cyclic voltammograms of α-Mn_2O_3/PEDOT:PSS (a) during initial 3 cycles and (c) during 3 cycles after 100 cycles at 100mA·g^{-1}. Cyclic voltammograms of bare α-Mn_2O_3 (b) during initial 3 cycles and (d) during 3 cycles after 100 cycles at 100mA·g^{-1}.

The cyclic voltammetry analysis showed detailed information on the electrochemical reaction of PEDOT:PSS. As shown in Figs. 8a and b, two strong cathodic peaks at 0.7 V and 0.25 V are observed in the first lithiation curves, corresponding to irreversible solid electrolyte interphase (SEI) formation and the electrochemical reduction of Mn_2O_3 with Li, respectively [21]. During the first delithiation step, one peak near 1.25 V corresponds to the oxidation of

manganese metal. The cathodic peak located at 0.25 V shifted to 0.35 V in the subsequent two scans, resulting from reconstruction which similarly occurred in the galvanostatic charge and discharge voltage profiles [21]. In the CV curves of α-Mn_2O_3/PEDOT:PSS, an obvious cathodic peak at 0.12 V and an anodic peak at 0.55 V might be assigned to the reversible formation of an SEI layer due to PEDOT:PSS; This SEI layer disappeared after 10 cycles [47,48]. Fig. 8b and d show CV curves of α-Mn_2O_3/PEDOT:PSS and α-Mn_2O_3/PEDOT:PSS after 100 cycles, respectively. For α-Mn_2O_3/PEDOT:PSS, there is reaction in the low voltage region as compared to the CV curves of α-Mn_2O_3 and another anodic peak at 2.1 V, which corresponds to the oxidation of Mn^{2+} to Mn^{4+}, which increases with repeating charge and discharge cycles [19,49].

Fig. 9a shows the XPS spectrum of Mn 2p for α-Mn_2O_3/PEDOT:PSS after 100 cycles. Two peaks at 643.87 and 655.27 eV are observed, which is characteristic of Mn^{4+}[19]. The X-ray absorption near-edge structure (XANES) spectra of the 10 cycled and 100 cycled α-Mn_2O_3/PEDOT:PSS electrode are shown in Fig. 10b, as well as a reference for manganese oxides. The corresponding XANES data are sensitive to the chemical and structural conditions of the material. Considering only the chemical condition, the XANES spectra indicate that the oxidation state of manganese in cycled α-Mn_2O_3/PEDOT:PSS is Mn^{2+} [50]. The oxidation states of both 100 cycled α-Mn_2O_3/PEDOT:PSS

and α-Mn_2O_3 nanowires is between +3 and +4. This further oxidation on cycling might contribute to increase capacity during cycling.

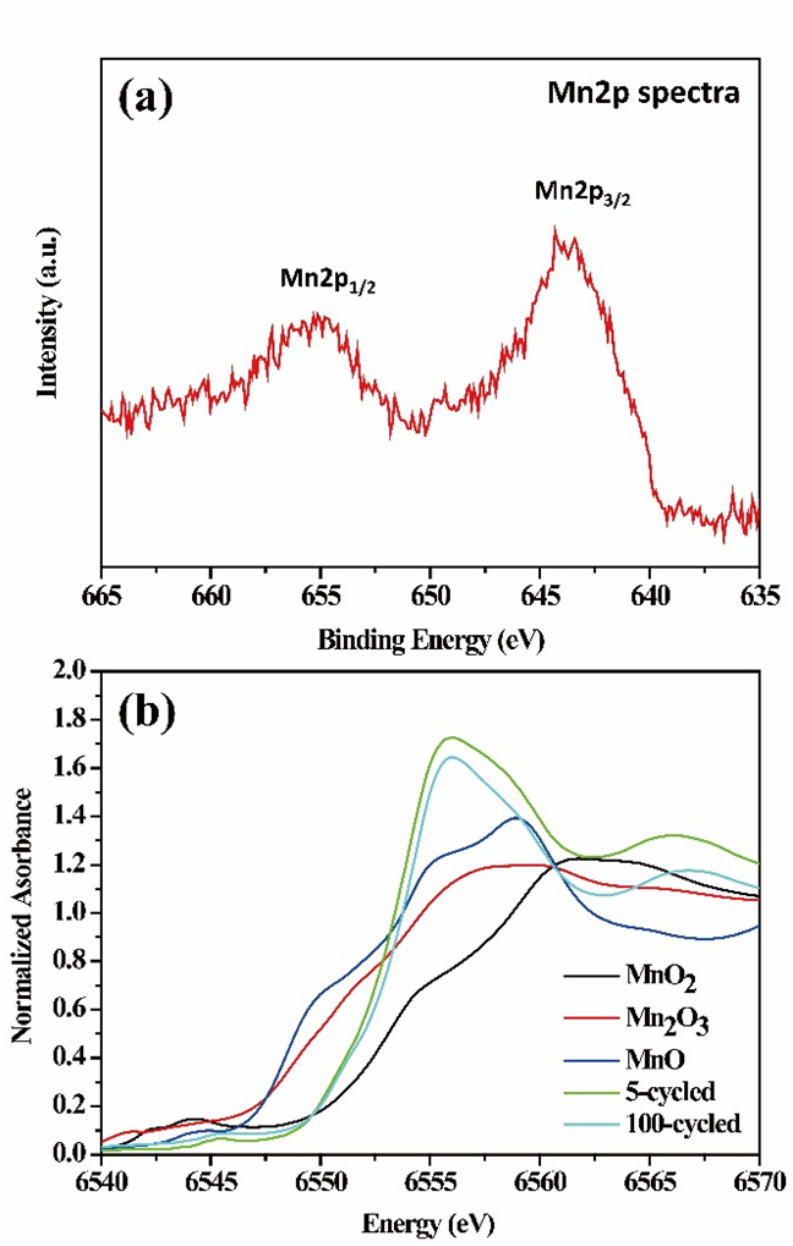

Figure 9. (a) XPS spectrum of 100 cycled α-Mn_2O_3/PEDOT:PSS at Mn 2p after washing with acetonitrile, (b) normalized Mn K-edge XANES spectrum of α-Mn_2O_3/PEDOT:PSS with reference spectra (MnO_2, Mn_2O_3 and MnO powder).

4. Conclusion

α-Mn_2O_3/PEDOT:PSS nanowires were prepared by synthesizing α-MnO_2 nanowire and coating PEDOT:PSS on the as-synthesized α-MnO_2 nanowire followed by heat treatment at 550 °C. α-Mn_2O_3/PEDOT:PSS nanowires showed significantly enhanced electrochemical performance in aspect of cycle stability and rate capability after coating PEDOT:PSS. In addition, α-Mn_2O_3/PEDOT:PSS nanowires exhibited much higher specific capacity than that of bare Mn_2O_3 nanowires and the capacity of Mn_2O_3/PEDOT:PSS nanowires reached about 1450 $mAh \cdot g^{-1}$ after 200 cycles at current density of 100 $mA \cdot g^{-1}$. The abnormal capacity increase on cycling might be due to multiple reasons such as reversible gel-like polymer layer growth on the surface and further oxidation of manganese oxide on cycling.

5. Reference

1. C. D. Rahn, C.-Y. Wang, Battery Systems Engineering, 1st edn (John Wiley & Sons, Ltd.). 2013.

2. M. Yoshio, R. J. Brodd, A. Kozawa, Lithium-Ion Batteries-Science and Technologies, 1st edn (Springer). 2009.

3. H. Li, Z. Wang, L. Chen, X. Huang, Research on Advanced Materials for Li-ion Batteries. *Adv. Mater*. 21 (2009) 4593-4607.

4. B. Ellis, K. T. Lee, L. F. Nazar, Positive Electrode Materials for Li-Ion and Li-Batteries. *Chem. Mater*. 22 (2010) 691-714.

5. J. B. Goodenough, K. S. Park, The Li-ion rechargeable battery: a perspective. *J. Am, Chem. Soc*. 135 (2013) 1167-76.

6. S.-W. Kim, D.-H. Seo, X. Ma, G. Ceder, K. Kang, Electrode Materials for Rechargeable Sodium-Ion Batteries: Potential Alternatives to Current Lithium-Ion Batteries. *Adv. Energy Mater*. 2 (2012) 710-721.

7. V. Palomares, P. Serras, I. Villaluenga, K.B. Hueso, J. Carretero-González, T. Rojo, Na-ion batteries, recent advances and present challenges to become low cost energy storage systems, *Energy Environ. Sci*. 5 (2012) 5884-5901.

8. H. Pan, Y.-S. Hu, L. Chen, Room-temperature stationary sodium-ion batteries for large-scale electric energy storage, *Energy Environ. Sci*. 6 (2013) 2338-2360.

9. G. Wang, L. Zhang, J. Zhang, A review of electrode materials for electrochemical supercapacitors, *Chem. Soc. Rev.* 41 (2012) 797-828.

10. V. Etacheri, R. Marom, R. Elazari, G. Salitra, D. Aurbach, Challenges in the development of advanced Li-ion batteries: a review, *Energy Environ. Sci*. 4 (2011) 3243-3262.

11. J. Liu, H. Xia, L. Lu, D. Xue, Anisotropic Co_3O_4 porous nanocapsules toward high-capacity Li-ion batteries, *J. Mater. Chem*. 20 (2010) 1506-1510.

12. B. Koo, H. Xiong, M.D. Slater, V.B. Prakapenka, M. Balasubramanian, P. Podsiadlo, C.S. Johnson, T. Rajh, E.V. Shevchenko, Hollow iron oxide nanoparticles for application in lithium ion batteries, *Nano Lett*. 12 (2012) 2429-2435.

13. X. Wang, X. Li, X. Sun, F. Li, Q. Liu, Q. Wang, D. He, Nanostructured NiO electrode for high rate Li-ion batteries, *J. Mater. Chem*. 21 (2011) 3571-3573.

14. M. Laurenti, N. Garino, S. Porro, M. Fontana, C. Gerbaldi, Zinc oxide nanostructures by chemical vapour deposition as anodes for Li-ion batteries, *J. Alloys Compd*. 640 (2015) 321-326.

15. M.-S. Park, Y.-M. Kang, G.-X. Wang, S.-X. Dou, H.-K. Liu, The Effect of Morphological Modification on the Electrochemical Properties of SnO_2 Nanomaterials, *Adv. Funct. Mater.* 18 (2008) 455-461.

16. S. Laruelle, S. Grugeon, P. Poizot, M. Dollé, L. Dupont, J-M. Tarascon, On the Origin of the Extra Electrochemical Capacity Displayed by MO/Li Cells at Low Potential, *J. Electrochem. Soc*. 149 (2002) A627-A634.

17. Y.-Y. Hu, Z. Liu, K.-W. Nam, O. J. Borkiewicz, J. Cheng, X. Hua, M. T. Dunstan, X. Yu, K. M. Wiaderek, L.-S. Du, K. W. Chapman, P. J. Chupas, X.-Q. Yang, C. P. Grey, Origin of additional capacities in metal oxide lithium-ion battery electrodes, *Nat. Mater*. 12 (2013) 1130–1136

18. W. Luo, X. Hu, Y. Sun, Y. Huang, Controlled synthesis of mesoporous MnO/C networks by microwave irradiation and their enhanced lithium-storage properties, *ACS Appl. Mater. Interfaces* 5 (2013) 1997-2003.

19. Y. Sun, X. Hu, W. Luo, F. Xia, Y. Huang, Reconstruction of Conformal Nanoscale MnO on Graphene as a High-Capacity and Long-Life Anode

Material for Lithium Ion Batteries, *Adv. Funct. Mater.* 23 (2013) 2436-2444.

20. M. Kundu, C.C. Ng, D.Y. Petrovykh, L. Liu, Nickel foam supported mesoporous MnO_2 nanosheet arrays with superior lithium storage performance, *Chem. Commun*. 49 (2013) 8459-8461.

21. X. Li, S. Xiong, J. Li, X. Liang, J. Wang, J. Bai, Y. Qian, MnO@carbon core-shell nanowires as stable high-performance anodes for lithium-ion batteries, *Chem. Eur. J.* 19 (2013) 11310-11319.

22. Z. Cai, L. Xu, M. Yan, C. Han, L. He, K.M. Hercule, C. Niu, Z. Yuan, W. Xu, L. Qu, K. Zhao, L. Mai, Manganese oxide/carbon yolk-shell nanorod anodes for high capacity lithium batteries, *Nano Lett*. 15 (2015) 738-744.

23. J.-G. Wang, C. Zhang, D. Jin, K. Xie, B. Wei, Synthesis of ultralong MnO/C coaxial nanowires as freestanding anodes for high-performance lithium ion batteries, *J. Mater. Chem. A*, 3 (2015) 13699-13705.

24. H. Jiang, Y. Hu, S. Guo, C. Yan, P.S. Lee, C. Li, Rational design of MnO/carbon nanopeapods with internal void space for high-rate and long-life li-ion batteries, *ACS Nano* 8 (2014) 6038-6046.

25. Y. Sun, X. Hu, W. Luo, Y. Huang, Porous carbon-modified MnO disks prepared by a microwave-polyol process and their superior lithium-ion storage properties, *J. Mater. Chem*. 22 (2012) 19190-19195.

26. Q. Hao, J. Wang, C. Xu, Facile preparation of Mn_3O_4 octahedra and their long-term cycle life as an anode material for Li-ion batteries, *J. Mater. Chem. A* 2 (2014) 87-93.

27. H. Li, P. Balaya, J. Maier, Li-Storage via Heterogeneous Reaction in Selected Binary Metal Fluorides and Oxides, *J. Electrochem. Soc*. 151 (2004) A1878-A1885.

28. Y.F. Zhukovskii, P. Balaya, E.A. Kotomin, J. Maier, Evidence for Interfacial-Storage Anomaly in Nanocomposites for Lithium Batteries from First-Principles Simulations, *Phys. Rev. Lett.* 96 (2006) 058302-058304.

29. Y. Deng, L. Wan, Y. Xie, X. Qin, G. Chen, Recent advances in Mn-based oxides as anode materials for lithium ion batteries, *RSC Adv*. 4 (2014) 23914-23935.

30. X. Liu, C. Chen, Y. Zhao, B. Jia, A Review on the Synthesis of Manganese Oxide Nanomaterials and Their Applications on Lithium-Ion Batteries, *J. Nanomater*. 2013 (2013) 1-7.

31. L. Mai, X. Tian, X. Xu, L. Chang, L. Xu, Nanowire electrodes for electrochemical energy storage devices, *Chem. Rev*, 114 (2014) 11828-11862.

32. Q. Li, L. Yin, Z. Li, X. Wang, Y. Qi, J. Ma, Copper doped hollow structured manganese oxide mesocrystals with controlled phase structure and morphology as anode materials for lithium ion battery with improved

electrochemical performance, *ACS Appl. Mater. Interfaces* 5 (2013) 10975-10984.

33. X. Wang, S. Qiu, G. Lu, C. He, J. Liu, L. Luan, W. Liu, Fabrication of porous MnO microspheres with carbon coating for lithium ion battery application, *CrystEngComm*. 16 (2014) 1802-1809.

34. Y. Zhang, Y. Yan, X. Wang, G. Li, D. Deng, L. Jiang, C. Shu, C. Wang, Facile synthesis of porous Mn_2O_3 nanoplates and their electrochemical behavior as anode materials for lithium ion batteries, *Chem. Eur. J*. 20 (2014) 6126-6130.

35. W. Zhao, N. Du, C. Xiao, H. Wu, H. Zhang, D. Yang, Large-scale synthesis of Ag–Si core–shell nanowall arrays as high-performance anode materials of Li-ion batteries, *J. Mater. Chem. A* 2 (2014) 13949-13954.

36. L. Groenendaal, F. Jonas, D. Freitag, H. Pielartzik, J. R. Reynolds, Poly(3,4-ethylenedioxythiophene) and Its Derivatives: Past, Present, and Future. *Adv. Mater*. 12 (2000**)** 481-494.

37. X. Wang, Y. Li, Selected-Control Hydrothermal Synthesis of α- and β-MnO_2 Single Crystal Nanowires, *J. Am. Chem. Soc*. 124 (2002) 2880-2881.

38. B. Ji, X. Jiao, N. Sui, Y. Duan, D. Chen, Long single-crystalline α-Mn_2O_3 nanowires: facile synthesis and catalytic properties, *CrystEngComm* 12 (2010) 3229-3234

39. T.T. Tung, T.Y. Kim, H.W. Lee, E. Kim, T.H. Lee, K.S. Suh, Conducting Nanocomposites Derived from Poly(styrenesulfonate)-Functionalized MWCNT-PSS and PEDOT, *J. Electrochem. Soc*. 156 (2009) K218-K222.

40. D. Chen, D. Chen, X. Jiao, Y. Zhao, Hollow-structured hematite particles derived from layered iron (hydro)oxyhydroxide-surfactant composites, *J. Mater. Chem*. 13 (2003) 2266–2270.

41. B. Gillot, M. E. Guendouzi, M. Laarj, Particle size effects on the oxidation-reduction behavior of Mn_3O_4 hausmannite, *Mater. Chem. Phys*. 70 (2001) 54-60.

42. P. A. Schultz, Shift in XPS levels in ionic adsorbate layers due to electrostatic effects, *Surf. Sci*. 209 (1989) 229-242.

43. K. Raj, J.A. Shanmugam, R. Mahalakshmi, R.B. Viswanathan, XPS and IR spectral studies on the structure of phosphate and sulphate modified titania - A combined DFT and experimental study, *Indian J. Chem. Sec. A* 49 (2010) 9-17.

44. D. Yonekura, E. Iwama, N. Ota, M. Muramatsu, M. Saito, Y. Orikasa, W. Naoi, K. Naoi, Progress of the conversion reaction of Mn_3O_4 particles as

a function of the depth of discharge, *Phys. Chem. Chem. Phys*. 16 (2014) 6027-6032.

45. P. Lu, C. Li, E.W. Schneider, S.J. Harris, Chemistry, Impedance, and Morphology Evolution in Solid Electrolyte Interphase Films during Formation in Lithium Ion Batteries, *J. Phys. Chem. C* 118 (2014) 896-903.

46. Z. Yang, Y. Feng, Z. Li, S. Sang, Y. Zhou, L. Zeng, An investigation of lithium intercalation into the carbon nanotubes by a.c. impedance, *J. Electroanal. Chem*. 580 (2005) 340-347.

47. Z. Chen, J.W.F. To, C. Wang, Z. Lu, N. Liu, A. Chortos, L. Pan, F. Wei, Y. Cui, Z. Bao, A Three-Dimensionally Interconnected Carbon Nanotube-Conducting Polymer Hydrogel Network for High-Performance Flexible Battery Electrodes, *Adv. Energy Mater*. 4 (2014) 1400207.

48. Y. Yao, N. Liu, M.T. McDowell, M. Pasta, Y. Cui, Improving the cycling stability of silicon nanowire anodes with conducting polymer coatings, *Energy & Environ Sci. 5* (2012) 7927-7930.

49. H. Xia, M. Lai, L. Lu, Nanoflaky MnO_2/carbon nanotube nanocomposites as anode materials for lithium-ion batteries, *J. Mater. Chem.* 20 (2010) 6896-6902.

50. M.A. Lowe, J. Gao, H.D. Abruña, In operando X-ray studies of the conversion reaction in Mn_3O_4 lithium battery anodes, *J. Mater. Chem. A* 1 (2013) 2094-2103.

51. L.-J. Her, J.-L. Hong, C.-C. Chang, Preparation and electrochemical characterizations of poly(3,4-dioxyethylenethiophene)/$LiCoO_2$ composite cathode in lithium-ion battery, J. Power Sources 157 (2006) 457-463.

52. C. Arbizzani1, M. Mastragostino, M. Rossi, Preparation and electrochemical characterization of a polymer $Li_{1.03}Mn_{1.97}O_4$/pEDOT composite electrode, Electrochem. Comm. 4 (2002) 545-549

53. X. Liu, H. Li, D. Li, M. Ishida, H. Zhou, PEDOT modified $LiNi_{1/3}Co_{1/3}Mn_{1/3}O_2$ with enhanced electrochemical performance for lithium ion batteries, J. Power Sources 243 (2013) 374-380.

54. L. Yue, S. Wang, X. Zhao, L. Zhang, Nano-silicon composites using poly(3,4- ethylenedioxythiophene):poly(styrenesulfonate) as elastic polymer matrix and carbon source for lithium-ion battery anode, J. Mater. Chem. 22 (2012) 1094-1099.

55. D.-L. Ma, Z.-Y. Cao, H.-G. Wang, X.-L. Huang, L.-M. Wang, X.-B. Zhang, Three-dimensionally ordered macroporous FeF_3 and its in situ homog-

enous polymerization coating for high energy and power density lithium ion batteries, Energy Environ. Sci. 5 (2012) 8538-8542.

6. Abstract (in Korean)

컨버젼 반응을 통해 리튬 이온을 저장하는 전이금속 산화물은 리튬 이온 배터리의 저장 물질로 널리 연구되고 있다. 하지만, 전이 금속은 충/방전 사이클을 거치면서 용량이 감소하는 데, 이러한 현상은 이 물질을 산업화 하는 데 걸림돌이 된다. 본 논문에서는 이러한 용량 감소를 해결하기 위해서, Mn_2O_3 나노와이어 물질에 전도성 고분자인 PEDOT:PSS (poly(3,4-ethylenedioxythiophene) polystyrene sulfonate)를 코팅하였다. 코팅된 PEDOT:PSS 는 표면의 저항을 감소시켰고, 충/방전 사이클을 거치면서 붕괴된 물질의 표면 사이에서 전자 경로를 제공하여 배터리 성능을 높였다.

α-Mn_2O_3/PEDOT:PSS 는 전류 밀도가 100 $mA \cdot g^{-1}$ 일 때, 200 사이클 이후에도 1450 $mAh \cdot g^{-1}$ 의 가역 용량을 보일 만큼 우수한 사이클 안정성을 보였다. 사이클에 다른 용량 증가는 다양한 산화수의 망간 산화물들과 망간 산화물 표면에서 생성된 겔과 같은 형태의 고분자의 가역적 반응에 의한 것으로 여겨진다. 이러한 결과는 PEDOT:PSS 가 전자

경로를 제공하고 충/방전 과정에 의해 생긴 물질의 붕괴를 막아주면서 전기화학적 활성을 증가 시킨 것을 설명해준다.

주요 핵심어 : 망간 산화물, PEDOT:PSS, 용량 증가, 컨버젼 반응, 리튬 저장 물질

Appendix

Fabrication of Three-Dimentionally Ordered Nickel Cobalt Sulfide Electrodes for Pseudocapacitor

1. Abstract

Three dimensionally ordered nickel cobalt sulfide electrode has been fabricated directly on stainless steel substrates as a current collector without binder or conducting agent. First, 350 nm silica nanoparticles dispersion is spin-coated on the stainless steel substrate to obtain three-dimensionally ordered silica template. And then SiO_2@nickel cobalt silicate core-shell structure was synthesized in aqueous solution of $Ni(NO_3)_2 \cdot 6H_2O$, $Co(NO_3)_2 \cdot 6H_2O$ and urea. The nickel cobalt silicate shell was converted into nickel cobalt sulfide through a hydrothermal reaction in the presence of Na_2S, where silica core are etched at the same time. The thickness of nickel cobalt silicate shell was changed by the concentration of nickel and cobalt precursor. Also, three-dimensional structure nickel cobalt sulfide was synthesized by proper quantity of sodium sulfide. The obtained nickel cobalt sulfide was characterized by Scanning Electron Microscopy (SEM), X-ray diffraction (XRD) and Electron dispersive spectroscopy (EDS).

2. Introduction

With the increase of the environment pollution, there are large development of field relating energy such as renewable energy, energy storage system (ESS), and so on. Besides, ESS is spotlighted because of development of electric vehicles (EVs). In recent, many researchers have been interested in electrochemical double layer capacitor (EDLC) or electrochemical supercapacitor (ES) due to high power density, long lifecycle, etc.

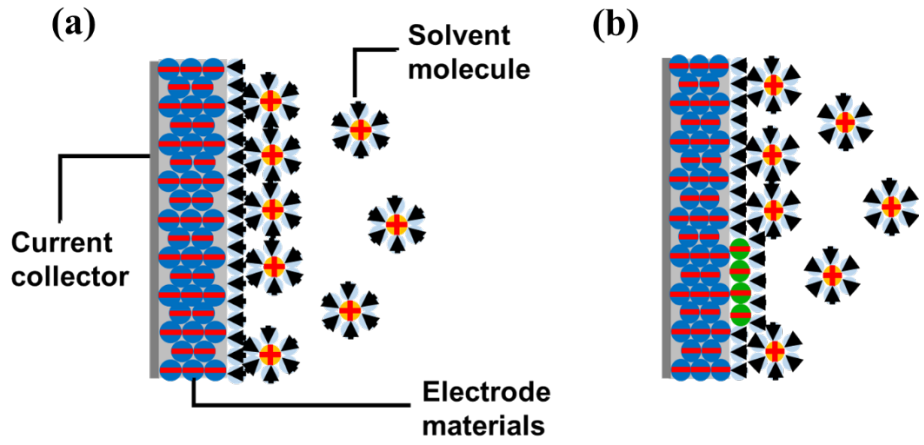

Figure A1. Principles of (a) EDLC (b) pseudocapacitor

There are two types of supercapacitor; **(1) EDLC** : Carbon based materials generally are used as electrode for EDLC. EDLC store energy in the electrolyte interfaces. Two electrolyte layer called “Helmholtz” double layer separate the charges between electrode materials and solvated opposite charged ions. The two opposite charged layer store the energy like conventional capacitor

and there is no charge transfer between electrode and adsorbed ion because they have only physical adsorption/desorption caused by electrostatic force not chemical bond. **(2) Pseudocapacitor** : unlike EDLC, pseudocapacitor stores electrical energy by reversible faradaic redox reaction. They have charge transfer between specific adsorbed ions and electrode materials. Transition metal oxides like RuO_2, IrO_2, and MnO_2 are used as electrode for pseudocapacitor. Normally, pseudocapacitor has larger capacitance than EDLC because they undergo faradaic redox reaction [1-3]. However, pseudocapacitor has poor structure and cycling stability comparing with EDLC because of the redox reaction of the electrode. Also, the poor conductivity of binder reduce performance, so many researchers challenge to fabricate binder-free supercapacitor electrode. For example, Huang et al. reported binder-free nickel based superpercapcitor electrode [4], and Lou et al. also made $NiCo_2O_4$ nanoneedle as binder-free supercapacitor electrode [5]. Especially, the three dimensional structure electrode attracted many interests as binder-free electrode [6]. Tang et al. and Liu et al. synthesized three-dimensionally ordered macroporous materials for supercapacitor [7-8]. In earliest pseudocapacitor research, RuO_2 is most actively studied but they are expensive and toxic. So, other transition metal oxides such as MnO_2, Ni_xO_y and Co_xO_y are rised as promising candidates for pseudocapacitor [1]. However the low intrinsic conductivity of metal oxide is still limitation as electrode for pseudocapacitor. To solve the problems things, doped-metal oxide or metal sulfide has been carried out recently due to their higher conductive characters [9-11]. Among

them, $NiCo_2S_4$ was attracted the researcher's interest because they have higher conductivity than other transition metal oxides and rich redox reaction [12-13]. And three-dimensionally structured materials have high surface area and effective ion diffusion path, so they have high rate capability, and excellent long-term cycle stability [14].

Here, we synthesized three-dimensional ordered structure $NiCo_2S_4$ and it did not use binder and any conductive agent. They have a tendency to vary thickness of shell by controlling amount of metal source. Furthermore, we found that the proper amount of sulfur source was needed for maintaining three-dimensional structure and the product has good potential to be material for supercapacitor.

3. Experimental section

Materials and Instruments

$Ni(NO_3)_2 \cdot 6H_2O$, $Co(NO_3)_2 \cdot 6H_2O$ and Na_2S purchased from Sigma-Aldrich. Tetraethyl orthosilicate (TEOS) purchased from TCI. And urea and NH_4OH purchased from Samchun Chemical Co. The morphologies of SiO_2, Ni-Co silicate and $NiCo_2S_4$ were confirmed by field emission scanning electron microscopy (FESEM, Hitachi S-4300). And the crystallographic phase of $NiCo_2S_4$ was identified by X-ray diffractometer (XRD, BRUKER MILLER Co., D8-Advance).

Synthesis of 350 nm SiO_2 nanoparticles

First, 10 mL of TEOS and 15 mL deionized water were mixed with 460 mL of 2-propanol. After 15 min stirring, 15 mL of NH_4OH was added dropwise and stirred overnight. Then, the white precipitation was washed with mixed solvent (H_2O : EtOH = 1 : 9, v/v) three times. And the precipitation was concentrated 800 mg/mL in the mixed solvent.

Spin coating on stainless steel (SUS) substrate

The circle stainless steel substrate with 1 cm diameter was attached with square glass. Then, the concentrated SiO_2 solution was dropped on the substrate and spun it 4,000 rpm for 1 min in spin coater. The coated substrates were annealed at 300 °C for 2 h due to more dense packing and better structure maintenance.

Synthesis of nickel cobalt silicate

The SiO_2 coated SUS substrate and 50 mg of urea were added in 5 mL of de-ionized water in glass vial. And nickel and cobalt mixture (Ni^{2+} : Co^{2+} = 1 : 2, n/n) was dissolved with three times weight of SiO_2 on substrate. Then, they were heated at 100 ºC for 12 h. After cooling, the substrate was washed with de-ionized water several times, and then nickel cobalt silicate on SUS substrate was obtained for next reaction.

Synthesis of nickel cobalt sulfide

The nickel cobalt silicate on SUS substrate was put in 5 mL of de-ionized water in Teflon-lined container. And Na_2S was dissolved 25 times more weight of nickel cobalt silicate on substrate. Then, they were reacted at 160 °C for 12 h in autoclave. The SUS substrate coated with dark-gray colored $NiCo_2S_4$ was washed with de-ionized water several times.

4. Result and Discussion

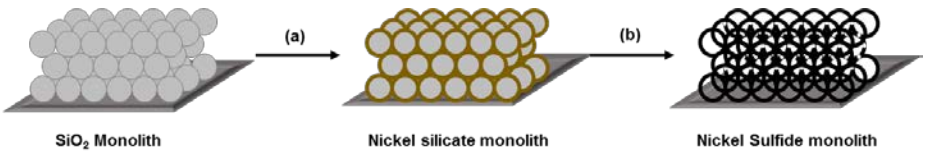

Scheme A1. Schematic illustrations of preparation of three-dimensionally ordered nickel cobalt sulfide. (a) Synthesis of nickel cobalt silicate shell on silica nanoparticles; (b) conversion to nickel cobalt sulfide with Na_2S.

In order to fabricate three-dimensionally ordered nickel cobalt sulfide directly on stainless steel substrate(SUS) as a current collector, first silica nanoparticles having diameters of 350 nm with a good size distribution were spin-coated on the SUS. And well-ordered template make more channel between particles and produce the stable electrodes. Therefore, the hexagonal packing was needed for ordered structure. The packing type was affected by viscosity and vapor pressure of solvent [15]. So, silica nanoparticles were dispersed in three types of solvent; (1) Type 1 (Only ethanol) (2) Type 2 (Butanol : ethylene glycol = 7 : 3, v/v), and (3) Type 3 (Ethanol : H_2O = 9 : 1, v/v). They showed different ordering trends by solvent type after spin coating.

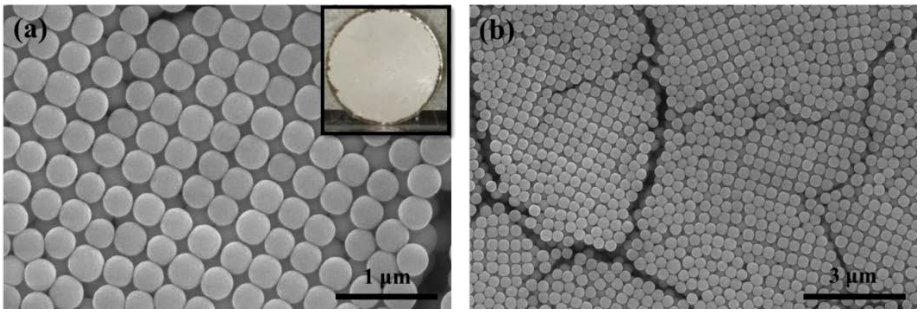

Figure A2. FE-SEM image of packing of SiO_2 nanoparticles in Type 1 (only ethanol) solvent. Inset is picture after spin coating.

SiO_2 nanoparticles formed cubic packing when they are in Type 1 solvent. Because ethanol solvent has low vapor pressure and ethanol was vaporized so fast, SiO_2 nanoparticles have no time to array hexagonal form. If SiO_2 nanoparticles have enough time to array, they would array hexagonal structure because the form is the most stable . But ethanol solvent had good affinity to SUS substrate, so SiO_2 nanoparticles were spin coated very well on SUS substrate.(Inset of **Fig. A2a**)

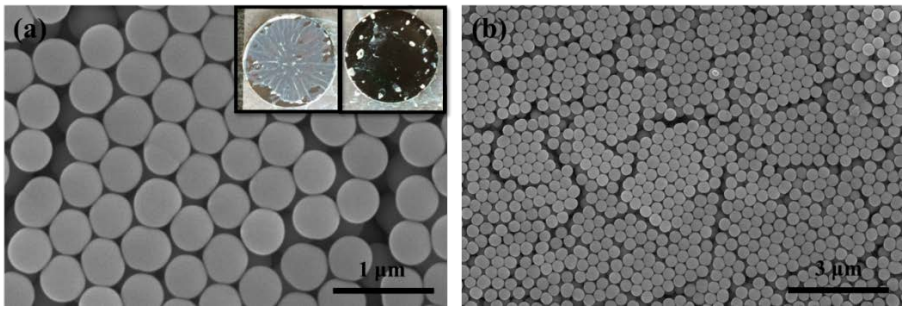

Figure A3. FE-SEM image of packing of SiO_2 nanoparticles in Type 2 (butanol : ethylene glycol = 7 : 3, v/v) solvent. Inset is picture after spin coating.

In Type 2 solvent, SiO_2 nanoparticles had hexagonal structure. Because butanol and ethylene glycol have low vapor pressure so they give enough time to array to SiO_2 nanoparticles. However, they also have high viscosity and poor adhesion with SUS substrate. As a result, SiO_2 nanoparticles were not spin coated well on SS substrate when they are in Type 2 solvent.(Inset of **Fig. A3a**)

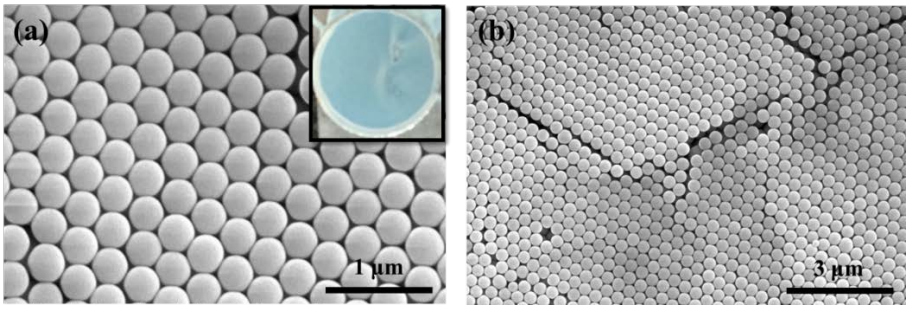

Figure A4. FE-SEM image of packing of SiO_2 nanoparticles in Type 3 (ethanol : H_2O = 9 : 1, v/v) solvent. Inset is picture after spin coating.

Considered packing and spin coating on substrate, proper vapor pressure, viscosity and adhesion with substrate are needed to make effective hexagonal ordered structure. When SiO_2 nanoparticles were dispersed in Type 3 solvent, they were spin coated very well and had perfect hexagonal packing. (**Fig.A4a**)

	Type I (Only EtOH)	Type II (BuOH : EG = 7:3)	Type III (EtOH : H_2O = 9:1)
packing	Cubic	Hexagonal	Hexagonal
Uniformity	O	X	O

Table A1. Packing and uniformity by solvent types.

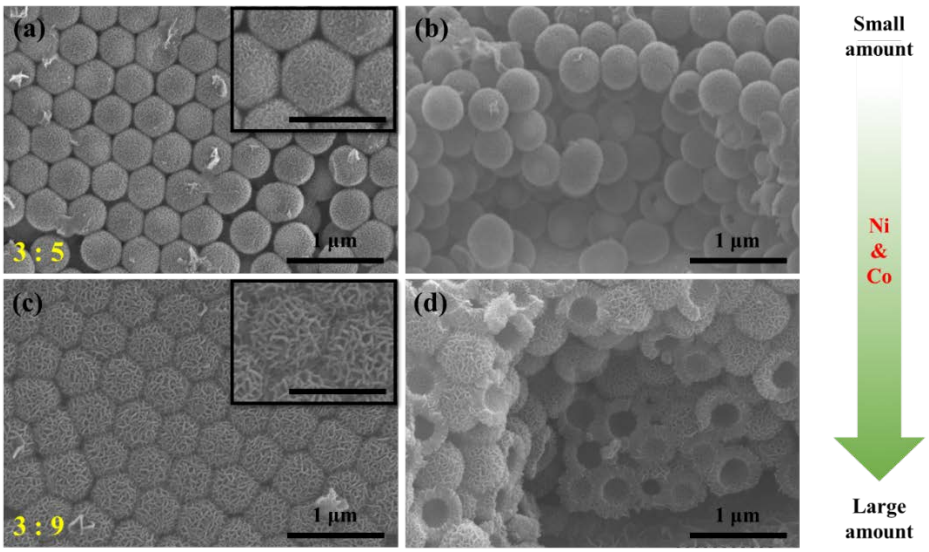

Figure A5. The morphologies of nickel cobalt silicate varying with nickel cobalt cation source. (a) FE-SEM top view (b) cross section view of nickel cobalt silicate when the ratio is 3 : 5 (SiO_2 : Ni/Co). (c) FE-SEM top view (d) cross section view of nickel cobalt silicate when the ratio is 3 : 9 (SiO_2 : Ni/Co). Scale bar of inset picture is 500 nm.

SiO_2 nano spheres were dissolved by urea to silicate anion, which produce nickel cobalt silicate through metal-ligand formation. SiO_2 nano spheres were activated by alkaline solution generated by the hydrolysis of urea [16-17]. Thickness nickel cobalt silicate shell was varied by the amount of nickel cobalt cation source. In Figure A5, the more the quantity of nickel and cobalt cation source, the thicker the nickel cobalt silicate shell.

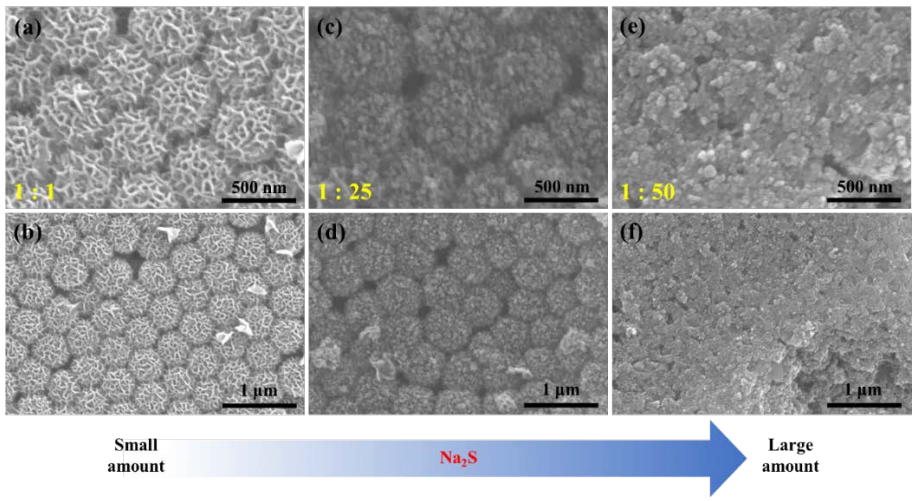

Figure A6. The trend of NCS varying with the amount of Na_2S. FE-SEM top view after reaction when the quantity of Na_2S is (a), (b) same (c), (d) 25 times (e), (f) 50 times.

In order to convert nickel cobalt silicate to nickel cobalt sulfide, SiO_2@nickel cobalt silicate was react with varying amount of Na_2S which serves as sulfurizing agent and silica template etching agent by generating basic environment [15]. When the amount of Na_2S is the same with nickel cobalt silicate, the sul-

fur substitution didn't happen because sulfur anion was running short to react sufficiently. Adding Na_2S with 25 times amount of nickel cobalt silicate, nickel cobalt sulfide were synthesized without structure decay. However, the structure was collapsed when the amount of Na_2S is 50 times. In water, Na_2S is decomposed to SH^- and OH^-; $Na_2S + H_2O \leftrightarrow 2Na^+ + SH^- + OH^-$ [15]. Therefore, excessive quantity of Na_2S made solvent too much basic and they etched SiO_2 core so fast before forming $NiCo_2S_4$ shell. (**Fig. A6**) The crystallinity of synthesized product was not good and they have $CoSO_4 \cdot 6H_2O$ because sulfur substitution was undergone in water. And the peak intensity of stainless steel is too high, so other peaks showed low intense, relatively. Although their crystallinity was not good, $NiCo_2S_4$ was well-synthesized. (**Fig. A7**)

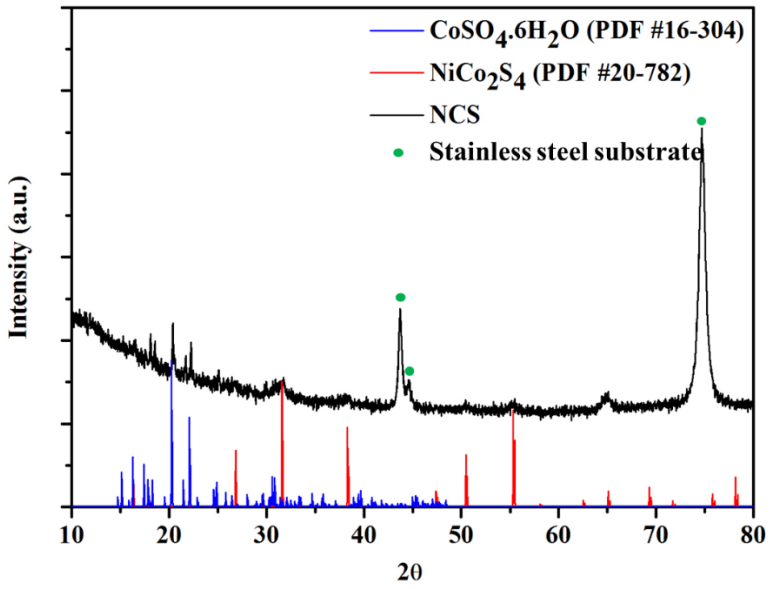

Figure A7. XRD patterns of synthesized NCS.

5. Conclusions

Three-dimensionally ordered nickel cobalt sulfide was successfully fabricated on stainless steel substrate for electrode of pseudocapacitor. Silica nano-spheres (nanoparticles?) were used as template for three-dimensionally ordered structures. The SiO_2 nanoparticles dispersions were spin-coated on stainless steel substrate and their packing morphology of nanoparticles was affected by the types of solvent that silica nano-spheres were arrayed hexagonal form in solvent consisting of water and ethanol. SiO_2@nickel cobalt silicate was obtained by reacting SiO_2 template with $Ni(NO_3)_2 \cdot 6H_2O$ and $Co(NO_3)_2 \cdot 6H_2O$. The thickness of nickel cobalt silicate increased with increasing the amount of metal ion sources. Nickel cobalt silicate were converted into nickel cobalt sulfide ($NiCo_2S_4$) in presence of Na_2S, and silica core was removed at the same time. Three-dimensional structure of $NiCo_2S_4$ was maintained by adjusting the amount of Na_2S. It is expected that this $NiCo_2S_4$ has high supercapacitive performance for pseudocapacitor.

6. References

1. G. Wang, L. Zhang, J. Zhang, A review of electrode materials for electrochemical supercapacitors, *Chem. Soc. Rev*., 41 (2012), 797-828

2. Y. Wang, Y. Xia, Recent progress in supercapacitor: From materials design to system construction, *Adv. Mater*., 25 (2013), 5336-5342

3. M. Winter, R. J. Brodd, What are batteries, fuel cells, and supercapacitors?, *Chem. Rev*., 104 (2004), 4245-4269

4. G. Zhang, W. Li, K. Xie, F. Yu, H. Huang, A one-step and binder-free method to fabricate hierarchical nickel-based supercapacitor electrodes with excellent performance, *Adv. Funct. Mater*, 23 (2013), 3675-3681

5. G. Q. Zhang, H. B. Wu, H. E. Hoster, M. B. Chan-Park, X. W. Lou, Single-crystalline $NiCo_2O_4$ nanoneedle arrays grown on conductive substrates as binder-free electrodes for high-performance supercapacitors, *Energy Environ. Sci*., 5 (2012), 9453-9456

6. Y. Li, L. Cao, M. Zhou, Y. Yang, P. Xiao, Y. Zhang, Ni-Co sulfide nanowires on nickel foam with ultrahigh capacitor for asymmetric

supercapacitors, *J. Mater. Chem. A*, 2 (2014), 6540-6548

7. W. Zhang, Y. Tan, Y. Gao, J. Wu, J. Hu, S. He, A. Stein, B. Tang, In_2O_3 nanoparticles on three-dimensionally ordered macroporous (3DOM) carbon for pseudocapacitor electrodes, *Electrochimica Acta*, 176 (2015), 861-867

8. Z. Liu, X. Tan, X. Gao, L. Song, Synthesis of three-dimensionally ordered macroporous manganese dioxide-carbon nanocomposites for supercapacitors, *Journal of Power Sources*, 267 (2014), 812-820

9. M. V. Reddy, G. V. Subba Rao, B. V. R. Chowdari, Metal oxides and oxysalts as anode materials for Li ion batteries, *Chem. Rev.*, 113 (2013), 5364-5457

10. J. Yang, X. Duan, Q. Qin, W. Zheng, Solvothermal synthesis of hierarchical flower-like ß-NiS with excellent electrochemical performance for supercapacitors, *J. Mater. Chem. A*, 1 (2013), 7880-7884

11. J. Xiao, L. Wan, S. Yang, F. Xiao, S. Wang, Design hierarchical electrodes with highly conductive $NiCo_2S_4$ nanotube arrays grown on carbon fiber paper for high-performance pseudocapacitors, *Nano Lett.*, 14 (2014), 831-838

12. H. Wan, J. Jiang, J. Yu, K. Xu, L. Miao, L. Zhang, H. Chen, Y. Ruan, $NiCo_2S_4$ porous nanotubes synthesis *via* sacrificial templates: high-performance electrode materials of supercapacitors, *CrystEngComm*., 15 (2013), 7649-7651

13. H. Chen, J. Jiang, L. Zhang, H. Wan, T. Qi, D. Xia, Highly conductive $NiCo_2S_4$ urchin-like nanostructures for high-rate pseudocapacitors, *Nanoscale*, 5 (2013), 8879-8883

14. M. J. Deng, P. J. Ho, C. Z. Song, S. A. Chen, J. F. Lee, J. M. Chen, K. T. Lu, Fabrication of Mn/Mn oxide core-shell electrodes with three-dimensionally ordered macroporous structures for high-capacitance supercapacitors, *Energy Environ. Sci*., 6 (2013), 2178-2185

15. A. Mihi, M. Ocaña, H. Míguez, Oriented colloidal-crystal thin films by spin-coating microspheres dispersed in volatile media, *Adv. Mater*., 18 (2006), 2244-2249

16. T. Zhu, Z. Wang, S. Ding, J. S. Chen, X. W. Lou, Hierarchical nickel sulfide hollow spheres for high performance supercapacitors, *RSC Adv*., 1 (2011), 397-400

17. J. Zheng, B. H. Wu, Z. Y. Jiang, Q. Kuang, X. L. Fang, Z. X. Xie, R. B. Huang, L. S. Zheng, General and facile synthesis of metal silicate

porous hollow nanostructures, *Chem. Asian. J.*, 5 (2010), 1439-1444

이학석사 학위 논문

α-Mn_2O_3 nanowires coated with conductive polymer for Li-ion battery anode materials : Synthesis, characterization, and applications

리튬 이온 이차전지의 음극 물질에 사용되는 전도성 고분자로 코팅된 알파 망간 옥사이드 나노 와이어의 합성 및 응용

2016 년 2 월

서울대학교 대학원

화학부 무기화학전공

김 성 준

M. S. Dissertation

α-Mn_2O_3 nanowires coated with conductive polymer for Li-ion battery anode materials : Synthesis, characterization, and applications

Supervisor : Professor Byeong-Hyeok Sohn

Major : Inorganic Chemistry

February 2016

By Seong-Jun Kim

Department of Chemistry

The Graduate School

Seoul National University

Abstract

α-Mn_2O_3 nanowires coated with conductive polymer for Li-ion battery anode materials : Synthesis, characterization, and applications

Seong-Jun Kim

Department of Chemistry, Inorganic Chemistry

The Graduate School

Seoul National university

Transition metal oxides have been considered as promising lithium storage materials that undergo a conversion reaction with Li ion, exhibiting high specific capacity. Among them, manganese oxides have high capacity compared to other metal oxides, and also their costs are inexpensive. However, capacity fading during cycling is the most serious obstacle for their commercialization. To slove the problems, poly(3,4-ethylenedioxythiophene) polystyrene sulfonate (PEDOT:PSS) was coated onto α-Mn_2O_3 nanowires while maintaining the structure of α-Mn_2O_3. PEDOT:PSS on the α-Mn_2O_3 reduced the resistance of the sur-

face and protected the surface electron channels from the pulverization effect of the charge–discharge operation. α-Mn_2O_3/PEDOT:PSS showed excellent cyclability with a reversible capacity of 1450 mAh·g^{-1} after 200 cycles at a current density of 100 mA·g^{-1}. An increase in capacity was observed with continuous cycling, which may be attributed to further oxidation of the manganese species and a reversible reaction of the gel-like polymer on the manganese surface. The results demonstrate that PEDOT:PSS enhances the electrochemical activity by providing electron channels and prevents pulverization caused by the charge and discharge process.

Keywords : manganese oxide, PEDOT:PSS, capacity increasing, abnormal capacity, lithium ion battery

Contents

List of figures scheme and tables

Figures

Scheme

Tables

Chapter 1.

α-Mn_2O_3 nanowires coated with conductive polymer for Li-ion battery anode materials : Synthesis, Characterization, and Applications

1. Introduction

Interest on electric vehicles (EVs) and energy storage systems is continuously increasing because of the depletion of fossil fuels and increasing environmental pollution [1-2]. Thus, many researchers have investigated a variety of energy storage devices such as lithium ion batteries (LIBs) [3-5], sodium ion batteries (NIBs) [6-8], and electrochemical capacitors [9]. There are three types of mechanisms reacting with Li ion according to anode materials. (1) An intercalation reaction, in which lithium ions are inserted to/removed from the host materials during charge–discharge cycles. For example, lithium ions are inserted to/removed from between a graphite lattice [$Li^+ + C_6 + e^- \leftrightarrow LiC_6$], (2) a reaction resulting from the alloying of Li metal with metal elements such as Sn, Ge, Sb, Zn, In, Bi, and Cd (Li_xM) , and (3) a “conversion” reaction (or redox reaction). Many transition metal oxides react with lithium ions ($MO_x + 2xLi+ + 2xe^- \leftrightarrow M + xLi_2O$) [10].

Many transition metal oxides can be easily prepared with various nanoscale morphologies and structures [11-15]. Moreover, these materials can exhibit even beyond the theoretical capacity calculated based on conversion reaction mechanism [11-13, 16-28]. It is reported that it can be explained by conjugate charge storage reactions which involve

space charge layer between lithium salts and metal surface [27-28], further oxidation of Mn^{2+} to Mn^{4+} in manganese oxides [19] and reversible formation of gel-like polymer [16].

Manganese-based oxides are considered promising anode materials for LIBs due to their high specific capacity, low toxicity, and low cost, and lower operating voltage than that of other conversion reaction-based materials such as Fe-, Co-, and Ni-based oxides [29]. Manganese oxides have various phases such as MnO, Mn_3O_4, MnO_2, and Mn_2O_3 [30]. Among the various morphologies, one-dimensional (1D) manganese oxide nanostructures such as nanowires (NWs) and nanotubes (NTs) have been studied for many energy applications. 1D nanostructured materials have advantages on facilitating electrical transport, and also effectively accommodates volume expansion. Also, they have short ion diffusion pathway, which enhances rate capability [31]. However, 1D nanostructured Mn_2O_3 has been rarely investigated in spite of its high theoretical capacity (1018 $mAh \cdot g^{-1}$) and many other advantages. Because intrinsic low electric conductivity of manganese oxides reduces its electrochemical performance. Thus, many advanced studies have been carried out to overcome these intrinsic problems. For example, Ma et al. doped copper into Mn_2O_3 [32] and Liu et al. coated carbon onto MnO particles to enhance conductivity of materials [33]. Wang et

al. controlled morphology by synthesizing Mn_2O_3 nanoplates [34]. Also, Yang et al. synthesized Ag–Si core–shell nanowall arrays using Ag cores as electron-conducting pathways, which enhanced the stability and conductivity of Si anodes [35].

Herein, a new composite of Mn_2O_3 nanowires and Poly(3,4-ethylenedioxythiophene) polystyrene sulfonate (PEDOT:PSS). PEDOT:PSS is a conductive polymer mixture. The PSS part carries a negative charge due to the deprotonated sulfonyl group and the PEDOT part has conjugated rings that carry a positive charge. PEDOT:PSS has very high conductivity (ca. 300 $S \cdot cm^{-1}$) and high stability [36]. Previously research shows that PEDOT:PSS coating on the cathode material can improve electronic conductivity of the electrode and electrochemical stability [51-53]. Her at al. and Arbizzani et al. prepared cathode materials using electrosynthesis of PEDOT and Yue et al. made nano-silicon/PEDOT:PSS composites for Li ion battery anode materials, but they have complex process to obtain their products due to polymerization step [51,52,54]. PEDOT:PSS also applied to 3DOM FeF3 which reacts through a conversion reaction. The novel 3DOM/PEDOT composite was synthesized by in-situ polymerization of 3,4-Ethylenedioxythiophene (EDOT) which secured both electron and ion channels [55]. Composite of carbonaceous materials/metal oxides de-

signed to improve the conductivity is usually synthesized in too reductive condition for maintaining structure of metal oxides. However, in our composite of α-Mn_2O_3 nanowires and PEDOT:PSS, α-Mn_2O_3 nanowires maintained its structure by virtue of a mild condition for PEDOT:PSS coating process. The nanosized metal oxides particles agglomerate together to stabilize their surface energy, which lead to poorly dispersed active materials during preparing slurry, while the nanowires is well distributed within the electrode. Thus, keeping the morphology of Mn_2O_3 NWs is important to enhance the electrochemical performance for the lithium ion battery. The PEDOT:PSS coated one-dimensional manganese oxides had improved the electronic conductivity, and enhanced stability of the electrochemical active sites.

2. Experimental Section

2.1 Synthesis of α-Mn_2O_3 nanowires

The synthesis method for α-MnO_2 nanowires was similar to the reported hydrothermal method [37]. Followed by, 7.35 g of $Mn(CH_3COO)_2{\cdot}4H_2O$ (0.03 mol) was dissolved in 80 mL of deionized water in a Teflon container, followed by the addition of 6.85 g of $(NH_4)_2S_2O_8$ (0.03 mol) and 7.94 g of $(NH_4)_2SO_4$ (0.06 mol). After thorough mixing, the solution was heated in an autoclave at 140 °C for 12 h. The resulting α-MnO_2 nanowires were collected

by centrifugation and washed three times with water and ethanol. The products were calcinated at 550 °C for 1.5 h.

2.2 Coating PEDOT:PSS onto α-Mn_2O_3 nanowires

300 mg of as-prepared α-Mn_2O_3 nanowires were dispersed in a co-solvent (27 mL of water and 270 mL of ethanol) in a round-bottom flask, followed by the addition of 3 mL of PEDOT:PSS solution (CLEVIOS™ P). The mixture was sonicated for 1 h at room temperature. After sonication, we collected the black precipitate by several rinse-centrifugation cycles. The precipitate was fully dried in vacuum for characterization.

2.3 Materials characterization

$Mn(CH_3COO)_2 \cdot 4H_2O$, $(NH_4)_2S_2O_8$ and $(NH_4)_2SO_4$ were purchased from SAMCHUN. PEDOT:PSS was purchased from Clevious™. Ethanol was purchased by J.T. Baker. The morphologies of α-Mn_2O_3 nanowires and α-Mn_2O_3/PEDOT:PSS were confirmed by transmission electron microscopy (TEM, Hitachi-7600) and field emission scanning electron microscopy (FESEM, Hitachi S-4300). The crystallographic phase of α-Mn_2O_3 was identified by X-ray diffractometer (XRD, D-MAX2500-PC). The diffraction data was collected in the 2 θ range of 10˚ ~ 80˚. Energy dispersive spectroscopy (EDS) mapping of α-Mn_2O_3/PEDOT:PSS was performed by high-resolution transmission electron microscopy (HRTEM, JEM-2100F, JEOL Ltd.). Thermogravimetric analysis (TGA, SDT-Q600, TA Instruments) and Fourier trans-

form infrared spectroscopy (FT-IR, Nicolet™ iS™10, Thermo scientific) were used to characterize the amount and presence of PEDOT:PSS, respectively. The shift of binding energy was assigned by X-ray photoelectron spectroscopy (XPS, AXIS-HIS, Kratos Inc.). X-ray absorption spectroscopy (XAS) analyses were performed at the 8C beam beamline of the Pohang Light Source (PLS). The cycled electrodes for XAS analyses were prepared by disassembling of the cells, washing them with diethyl carbonate, and drying them. Finally, the electrodes were sealed with Kapton® tape. All preparation processes were carried out in an argon-filled glove box.

2.4 Electrochemical measurements

The working electrode was prepared by coating a slurry containing active material (70 wt%), Super P (as a conductive agent, 20 wt%), and polyvinylidene fluoride (PVDF, 10 wt%) onto copper foil. The coated electrodes were dried under vacuum at 120 °C for 12 h and then pressed. The electrochemical performance of the active material was examined using CR2032 button cells consisting of the as-prepared electrode, a polypropylene separator, lithium foil as the counter electrode, and 1 M $LiPF_6$ in a mixture of ethylene carbonate (EC) and ethyl carbonate (DEC) (v/v = 50:50) as the electrolyte. The cells were assembled in an argon atmosphere glove box. A WBCS3000 cycler (WonA Tech, Korea) was employed for the galvanostatic charge–discharge experiment in a voltage range of 0.01–3 V versus Li^+/Li and for cyclic voltammetry (CV) measurements from 3 to 0.01 V versus Li^+/Li at a scan rate of 0.1 $mV \cdot s^{-1}$

at room temperature. Electrochemical impedance spectroscopy (EIS) was conducted in the frequency range from 100 kHz to 0.01 Hz with an AC signal amplitude of 5 mV (Autolab, PGSTAT128N)

3. Result and discussion

3.1 Synthesis and characterization of materials

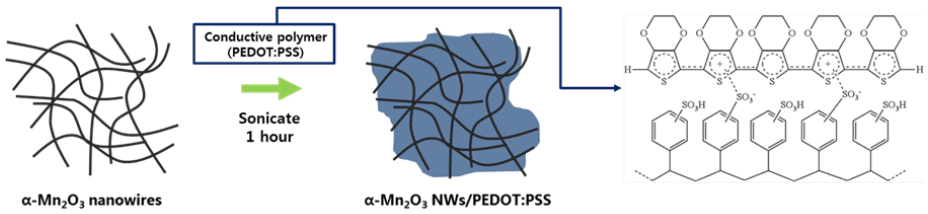

Figure 1. Schematic representation of the synthesis of α-Mn_2O_3/PEDOT:PSS.

α-MnO_2 nanowires were synthesized through a cation template-assisted hydrothermal method. These α-MnO_2 nanowires transformed into α-Mn_2O_3 at 550 °C or more in air. Fig. 1 shows the process of coating PEDOT:PSS onto the α-Mn_2O_3 nanowires. After heat treatment of as-prepared α-Mn_2O_3 nanowires at 550 °C in air, PEDOT:PSS was added to the nanowires via sonication. α-Mn_2O_3/PEDOT:PSS was obtained after 1 h in sonication. Cosolvent of DI waterand ethhanol should be used for this process. α-Mn_2O_3 nanowires have good dispersibility in ethanol but they don't in water because most hydroxyl groups on surface were eliminated during calcination. Howev-

er, PEDOT:PSS cannot disperse in ethanol but in water. So, Mn_2O_3 nanowires and PEDOT:PSS need proper ratio of two solvent. Therefore, the ratio 9 : 1 (ethanol : water, v/v) was identified as ideal ratio from dispersibility test. (**Fig. 2**)

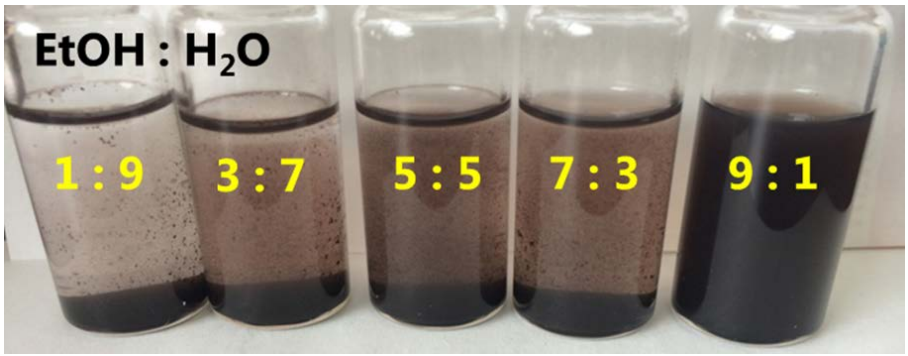

Figure 2. Dispersibility of α-Mn_2O_3 nanowires according as Ethanol/H_2O ratio.

The morphology of bare α-Mn_2O_3 nanowires are shown in TEM and SEM images (Fig. 3a-c). The prepared α-MnO_2 nanowires have 1D nanostructure with a diameter of 20 nm. The obtained α-Mn_2O_3 nanowires after heat treatment at 550 ℃ (or higher temperature) maintained their morphology even though the structures are changed. Furthermore, the morphology of α-Mn_2O_3 was still maintained after the coating process. Unlike a carbon-coating process, the PEDOT:PSS-coating process can omit heat treatment at high temperature, which

causes morphology change with a phase transition. The mild conditions of the PEDOT:PSS coating process has a significant advantage for applying conductive coatings onto electric materials.

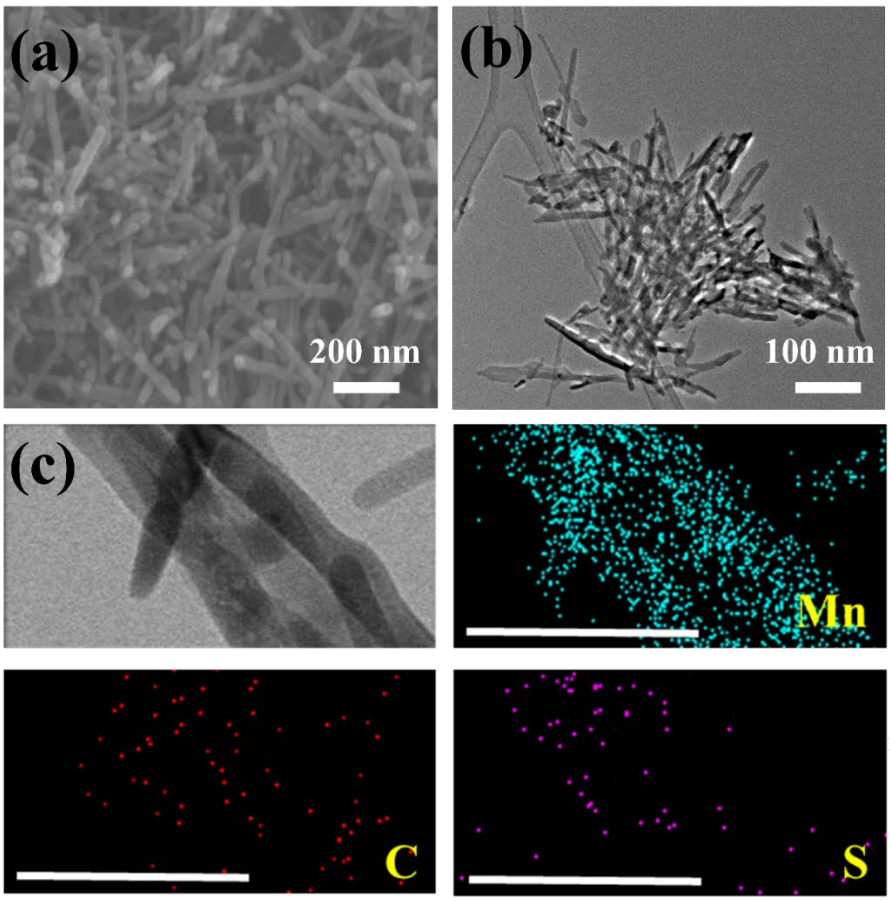

Figure 3. (a) FE-SEM and (b) TEM image of bare α-Mn_2O_3 nanowires. (c) TEM image (first picture) and EDS-mapping of bare α-Mn_2O_3 nanowires (scale bar is 200 nm)

The existence of PEDOT:PSS was characterized after the coating process by SEM, TEM, and EDS mapping (Fig. 4a-c) It is clearly seen that the diameter of α-Mn_2O_3/PEDOT:PSS nanowires is thicker than that of α-Mn_2O_3 nanowires (Fig. 4a). In addition, the coating of PEDOT:PSS on α-Mn_2O_3 nanowires is observed in TEM and EDS mapping (Fig. 4b and c). The XRD patterns of α-MnO_2 and the α-Mn_2O_3 nanowires were well matched with α-MnO_2 phase (PDF#44-0141) and α-Mn_2O_3 phase (PDF#24-508), respectively (Fig. 4d)

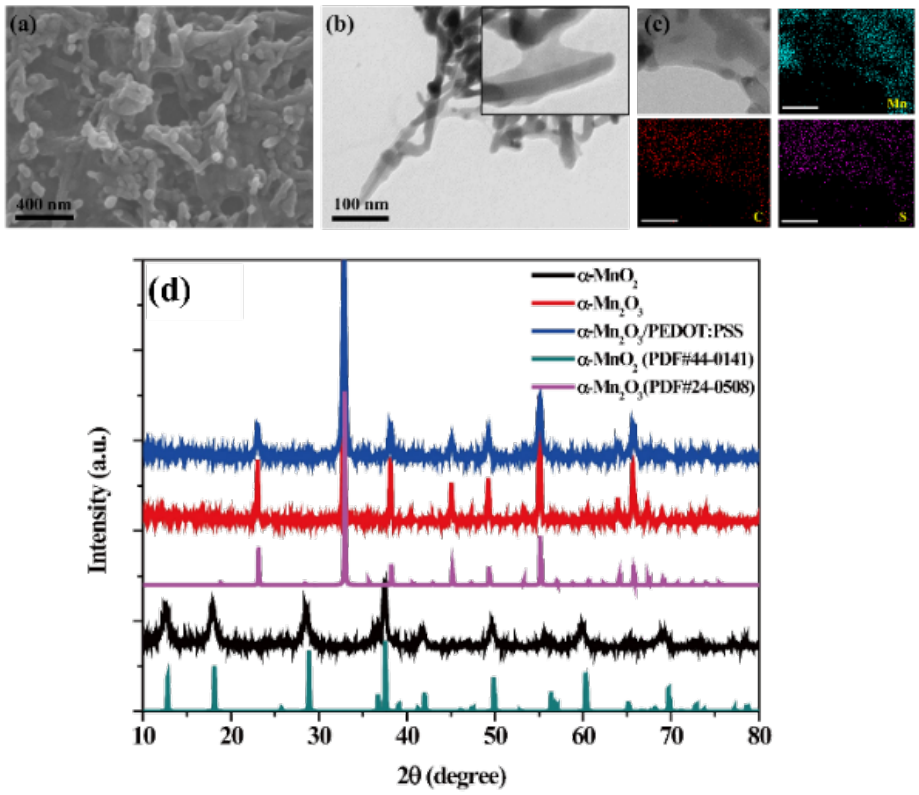

Figure 4. (a) FE-SEM and (b) TEM image of α-Mn_2O_3/PEDOT:PSS (c) EDS-mapping of α-Mn_2O_3/PEDOT:PSS (d) XRD patterns of α-MnO_2, bare α-Mn_2O_3 and α-Mn_2O_3/PEDOT:PSS.

According to TGA, approximately 23 % PEDOT:PSS was contained in α-Mn_2O_3/PEDOT:PSS nanowires (Fig. 5a). Also, the weight of bare α-Mn_2O_3 decreased because of its phase transition from α-Mn_2O_3 to Mn_3O_4, the removal of water from the surface hydroxyls, and the de-composition of a slight amount of SO_4^{2-} species on the surface [38]. The surface chemical species of α-Mn_2O_3/PEDOT:PSS and bare α-Mn_2O_3 were verified by FT-IR. α-Mn_2O_3/PEDOT:PSS exhibited unique peaks of PEDOT:PSS from 3500 to 3000 cm^{-1} and from 1700 to 750 cm^{-1} (Fig. 5b) [39]. Peaks indicating SO_4^{2-} anions (1260 to 900 cm^{-1}) and –OH groups from the adsorbed water and surface hydroxyls (~3400 and ~1600 cm^{-1}) were also found [40]. Both spectra showed peaks corresponding to the vibration of the Mn-O bond in Mn_2O_3 [41].

We further analyzed the chemical and oxidation states on surface of both materials by XPS. Binding energy shifts to lower appeared in both Mn 2p and O 1s spectra after coating (Fig. 5c and d, respectively). In addition, Messmer et al. reported that the electrostatic contribution affects binding energies [42]. The electrostatic interaction reduced the

binding energies of the Mn-O bond in the α-Mn_2O_3 nanowires. After addition of PEDOT:PSS, the two peaks of Mn 2p shifted to lower binding energy about 0.4 eV (642.4 → 642.0 eV and 654.4 → 654.0 eV, respectively) and the peaks of O 1s shifted 0.4 and 0.1 eV (530.8 → 530.4 eV and 532.2 → 532.1 eV), respectively. These O 1s peaks were caused by the presence of the S-O bond in the SO_4^{2-} anion and the adsorbed water on the surface [43].

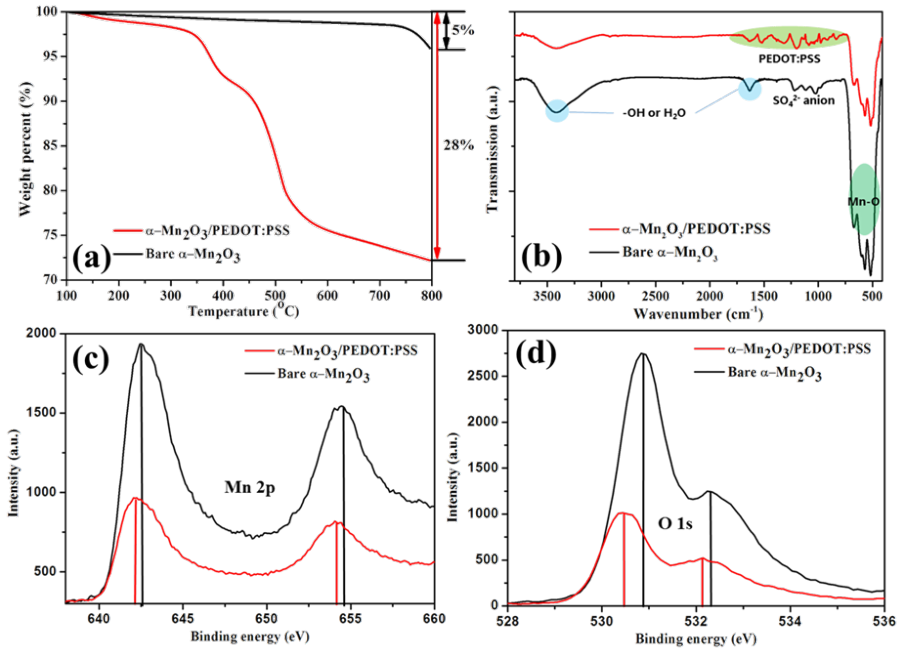

Figure 5. (a) TG analysis before and after treatment of PEDOT:PSS. (10 ℃ /min, Air condition) (b) FT-IR spectra before and after treatment of PEDOT:PSS. XPS spectras of the (c) Mn and (d) O atoms in materials before and after treatment of PEDOT:PSS.

Polythiophene group of PEDOT has positive charge that may help to attach on surface of α-Mn_2O_3 nanowires because surface charge of α-Mn_2O_3 nanowires is negative charge. (Fig 6) Two materials were attached by electrostatic interaction. Besides, sulfate anions on the surface interacted with PEDOT:PSS and they also help to stick between them.

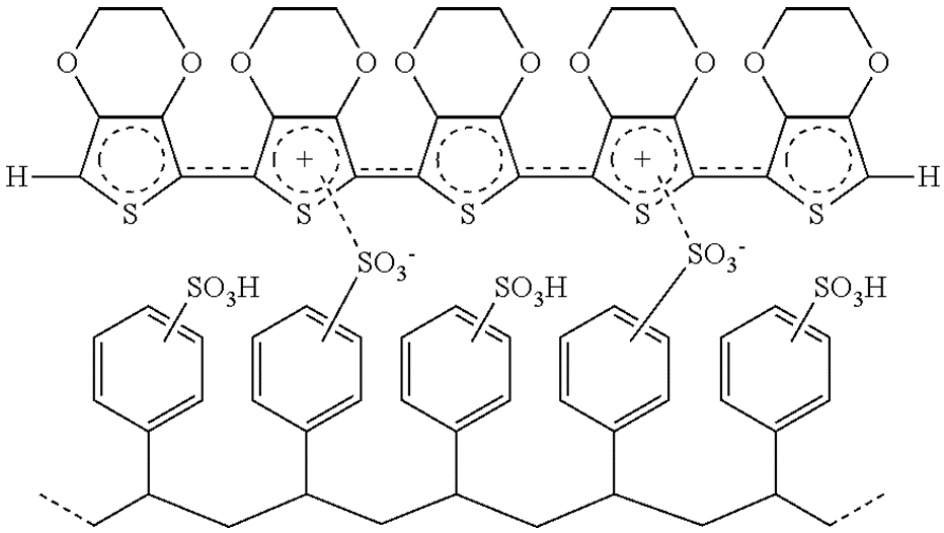

Figure 6. Illustration of PEDOT:PSS structure.

The surface potential of bare α-Mn_2O_3 nanowires is approximately -38.6 mV. After adding PEDOT:PSS, their surface charge shifts positive a little about -10.5 mV. (Table 1) PEDOT:PSS could lower the surface charge of bare α-Mn_2O_3 nanowires.

	Bare α-Mn_2O_3 NWs	α-Mn_2O_3 NW/PEDOT:PSS
1st	-41.0 mV	-9.99 mV
2nd	-37.5 mV	-11.0 mV
3rd	-37.4 mV	-10.6 mV
Average	**-38.6 mV**	**-10.5 mV**

Table 1. Zeta potential of bare α-Mn_2O_3 nanowires and α-Mn_2O_3/PEDOT:PSS.

3.2 Electrochemical performance in Li ion battery

The electrochemical performance was evaluated by galvanostatic charge and discharge measurements. Fig. 7a shows the cycle performance of α-Mn_2O_3/PEDOT:PSS and α-Mn_2O_3 at current density of 100 $mA \cdot g^{-1}$ in a potential range between 0.01 and 3 V. The specific capacities of α-Mn_2O_3/PEDOT:PSS and α-Mn_2O_3 decreased during initial several cycles [23]. However, the capacity of α-Mn_2O_3/PEDOT:PSS gradually increased after 25 cycles. The capacity reached a maximum value of 1450 $mAh \cdot g^{-1}$ after 200 cycles, whereas the capacity of α-Mn_2O_3 still under 400 $mAh \cdot g^{-1}$ after 200 cycles even though the capacity continuously increases after about 40 cycles. At higher current density, fluctuation on cycle performance was also observed. The capacity of α-Mn_2O_3/PEDOT:PSS decreased up to the 50th cycle and then started to rebound at 500 $mA \cdot g^{-1}$. These abnormal trends of increasing capacity after decreasing were further investigated through charge-discharge voltage profiles. Fig. 7c and d show the charge and discharge curves of α-Mn_2O_3/PEDOT:PSS and α-Mn_2O_3, respectively. Both α-Mn_2O_3/PEDOT:PSS and α-Mn_2O_3 show the typical lithiation and delithiation profiles of manga-

nese oxide. The first lithiation curves can be explained by dividing it into three distinct regions [44]. The first region was caused by the insertion of lithium ions into Mn_2O_3 to form $LiMn_2O_3$, followed by the diffusion of oxygen and lithium ions out of $LiMn_2O_3$ to form MnO, resulting in two quasi-plateaus above 0.3 V. The second region is an extended plateau near 0.3 V, resulting in the largest charge. The second region is related to the transformation from MnO into Mn metal and Li_2O. Finally, the third region is a sloping voltage below 0.3 V, which can be explained by interfacial insertion (or space charges). In the subsequent delithiation process, the oxidation of metallic manganese to MnO (not to Mn_2O_3) and the diffusion of lithium ions out of Li_2O occurred, which resulted in a plateau near 1.25 V. In the second lithiation process, the extended plateau near 0.3 V corresponding to the reduction of MnO to Mn^0 shifted to 0.45 V. This indicated that the obstacle of second lithiation is lower than that of the first lithiation as a result of formation of nanoscale metal cluster (<5 nm) imbedded in Li_2O matrix during the first lithiation [19]. In the lithiation curves of α-Mn_2O_3/PEDOT:PSS, main reaction occurs at plateau (0.45 V), which is related to the transformation of MnO to Mn up to 50 cycles. After 50 cycles, however, the plateau near 0.45 V gradually disappears, whereas the slope below 0.45 V gradually expands. It seems that the reaction in end of lithiation (below 0.45 V) is related to formation of gel-like polymer which is caused by pulverized nano-metal particles [16]. EIS analysis was introduced to investigate the effect of the PEDOT:PSS coating (Fig. 7e). The proposed equivalent circuits are a simplification of the real situation based on

several assumptions [45,46]. Although the α-Mn_2O_3/PEDOT:PSS electrode did not perfectly agree with the assumptions, the experimental values were consistent with the calculated data. Fig. 7e shows the Nyquist plots of α-Mn_2O_3 after 50 cycles and α-Mn_2O_3/PEDOT:PSS after 50 and 100 cycles. The equivalent circuits is presented in Fig. 7e, where R_o indicates ohmic resistance and R_f and C_f indicate the resistance of the SEI film and the capacity of the surface-passivating layer, respectively. The resistance of the charge transfer reaction and the capacitance of the double layer are represented by R_c and C_c, respectively. The values of R_o and R_f for α-Mn_2O_3/PEDOT:PSS (1.02 and 24.77 Ω, respectively) after 50 cycles were lower than the those of α-Mn_2O_3 (2.25 and 84.56 Ω, respectively). Furthermore, R_o and R_f of α-Mn_2O_3/PEDOT:PSS after 100 cycles displays lower values. This improvement is due to the coating of conductive PEDOT:PSS onto the α-Mn_2O_3 nanowire surface, which provided electron channel and served as a favorable binder agent for electrochemical microstructure reconstruction. However, the R_c value of α-Mn_2O_3 (29.78 Ω) is slightly increased after the coating (38.23 Ω for α-Mn_2O_3/PEDOT:PSS). As shown in Fig. 7f, rate performance of α-Mn_2O_3/PEDOT:PSS nanowires is also higher than that of α-Mn_2O_3 nanowires.

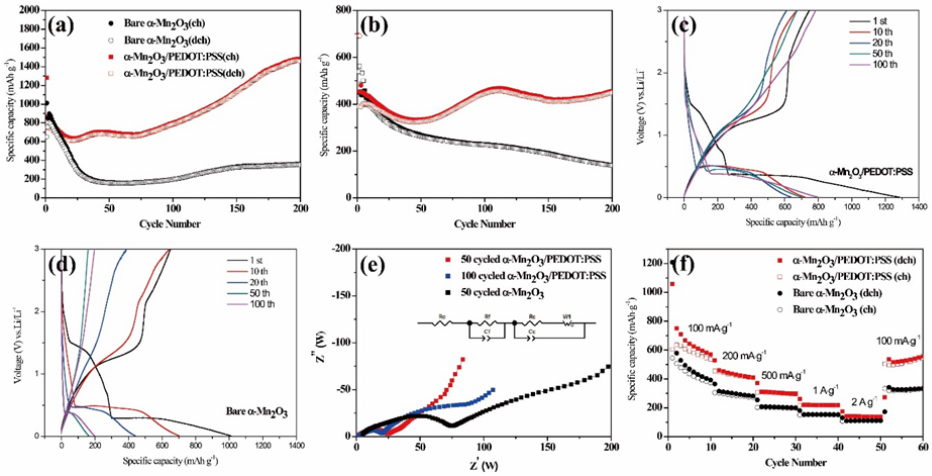

Figure 7. Cycle performances of bare α-Mn_2O_3 and α-Mn_2O_3/PEDOT:PSS at a current density of (a) 100 mA·g^{-1} and (b) 500 mA·g^{-1}. Voltage profiles of (c) α-Mn_2O_3/PEDOT:PSS and (d) α-Mn_2O_3. (e) AC impedance of α-Mn_2O_3/PEDOT:PSS and α-Mn_2O_3 with equivalent circuit. (f) Rate properties of α-Mn_2O_3/PEDOT:PSS.

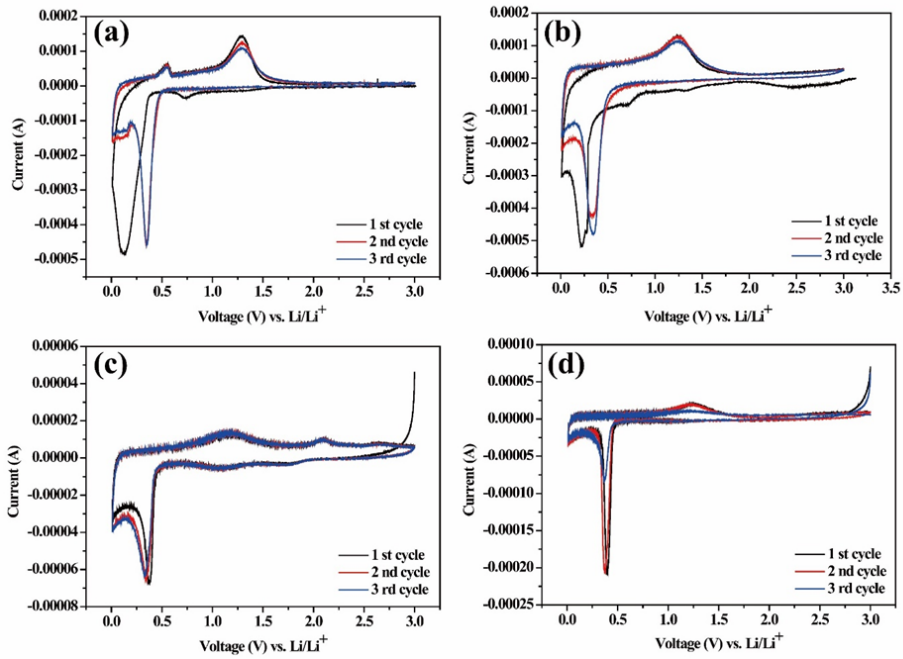

Figure 8. Cyclic voltammograms of α-Mn_2O_3/PEDOT:PSS (a) during initial 3 cycles and (c) during 3 cycles after 100 cycles at 100mA·g^{-1}. Cyclic voltammograms of bare α-Mn_2O_3 (b) during initial 3 cycles and (d) during 3 cycles after 100 cycles at 100mA·g^{-1}.

The cyclic voltammetry analysis showed detailed information on the electrochemical reaction of PEDOT:PSS. As shown in Figs. 8a and b, two strong cathodic peaks at 0.7 V and 0.25 V are observed in the first lithiation curves, corresponding to irreversible solid electrolyte interphase (SEI) formation and the electrochemical reduction of Mn_2O_3 with Li, respectively [21]. During the first delithiation step, one peak near 1.25 V corresponds to the oxidation of

manganese metal. The cathodic peak located at 0.25 V shifted to 0.35 V in the subsequent two scans, resulting from reconstruction which similarly occurred in the galvanostatic charge and discharge voltage profiles [21]. In the CV curves of α-Mn_2O_3/PEDOT:PSS, an obvious cathodic peak at 0.12 V and an anodic peak at 0.55 V might be assigned to the reversible formation of an SEI layer due to PEDOT:PSS; This SEI layer disappeared after 10 cycles [47,48]. Fig. 8b and d show CV curves of α-Mn_2O_3/PEDOT:PSS and α-Mn_2O_3/PEDOT:PSS after 100 cycles, respectively. For α-Mn_2O_3/PEDOT:PSS, there is reaction in the low voltage region as compared to the CV curves of α-Mn_2O_3 and another anodic peak at 2.1 V, which corresponds to the oxidation of Mn^{2+} to Mn^{4+}, which increases with repeating charge and discharge cycles [19,49].

Fig. 9a shows the XPS spectrum of Mn 2p for α-Mn_2O_3/PEDOT:PSS after 100 cycles. Two peaks at 643.87 and 655.27 eV are observed, which is characteristic of Mn^{4+}[19]. The X-ray absorption near-edge structure (XANES) spectra of the 10 cycled and 100 cycled α-Mn_2O_3/PEDOT:PSS electrode are shown in Fig. 10b, as well as a reference for manganese oxides. The corresponding XANES data are sensitive to the chemical and structural conditions of the material. Considering only the chemical condition, the XANES spectra indicate that the oxidation state of manganese in cycled α-Mn_2O_3/PEDOT:PSS is Mn^{2+} [50]. The oxidation states of both 100 cycled α-Mn_2O_3/PEDOT:PSS

and α-Mn_2O_3 nanowires is between +3 and +4. This further oxidation on cycling might contribute to increase capacity during cycling.

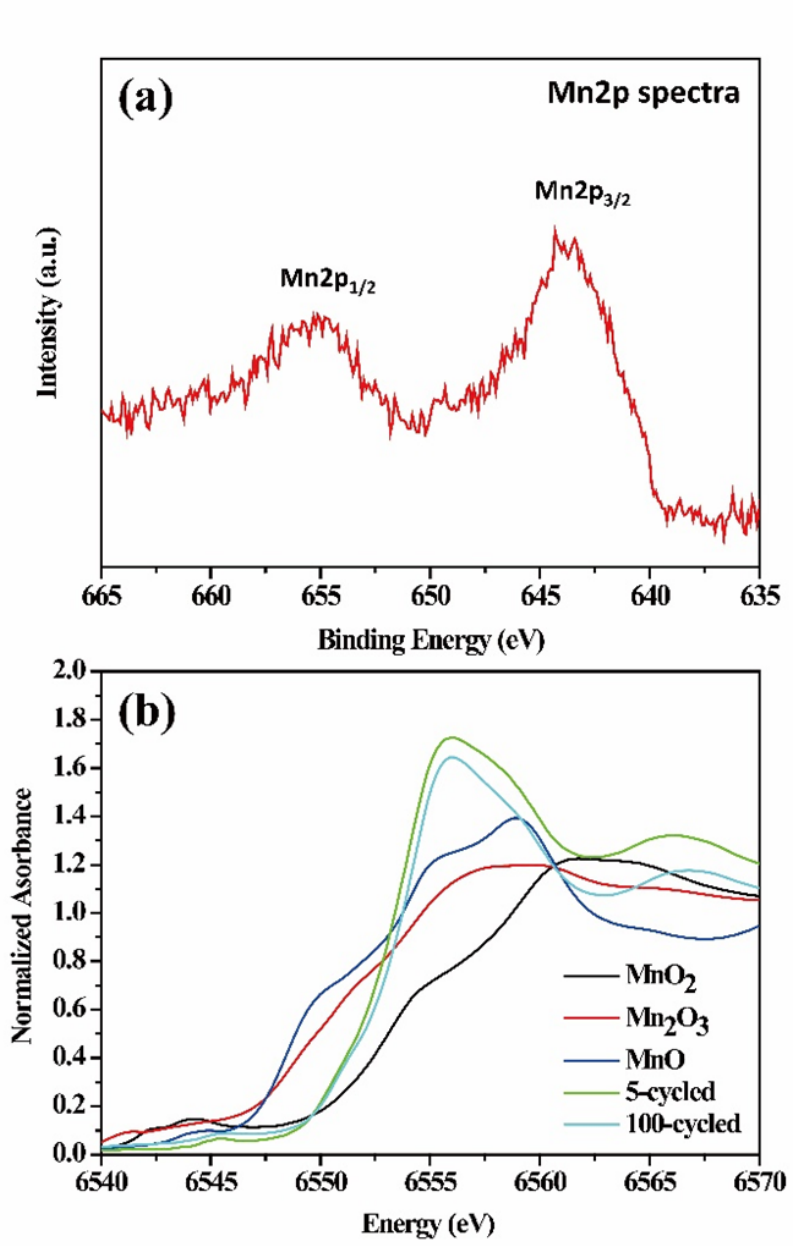

Figure 9. (a) XPS spectrum of 100 cycled α-Mn_2O_3/PEDOT:PSS at Mn 2p after washing with acetonitrile, (b) normalized Mn K-edge XANES spectrum of α-Mn_2O_3/PEDOT:PSS with reference spectra (MnO_2, Mn_2O_3 and MnO powder).

4. Conclusion

α-Mn_2O_3/PEDOT:PSS nanowires were prepared by synthesizing α-MnO_2 nanowire and coating PEDOT:PSS on the as-synthesized α-MnO_2 nanowire followed by heat treatment at 550 °C. α-Mn_2O_3/PEDOT:PSS nanowires showed significantly enhanced electrochemical performance in aspect of cycle stability and rate capability after coating PEDOT:PSS. In addition, α-Mn_2O_3/PEDOT:PSS nanowires exhibited much higher specific capacity than that of bare Mn_2O_3 nanowires and the capacity of Mn_2O_3/PEDOT:PSS nanowires reached about 1450 $mAh \cdot g^{-1}$ after 200 cycles at current density of 100 $mA \cdot g^{-1}$. The abnormal capacity increase on cycling might be due to multiple reasons such as reversible gel-like polymer layer growth on the surface and further oxidation of manganese oxide on cycling.

5. Reference

1. C. D. Rahn, C.-Y. Wang, Battery Systems Engineering, 1st edn (John Wiley & Sons, Ltd.). 2013.

2. M. Yoshio, R. J. Brodd, A. Kozawa, Lithium-Ion Batteries-Science and Technologies, 1st edn (Springer). 2009.

3. H. Li, Z. Wang, L. Chen, X. Huang, Research on Advanced Materials for Li-ion Batteries. *Adv. Mater*. 21 (2009) 4593-4607.

4. B. Ellis, K. T. Lee, L. F. Nazar, Positive Electrode Materials for Li-Ion and Li-Batteries. *Chem. Mater*. 22 (2010) 691-714.

5. J. B. Goodenough, K. S. Park, The Li-ion rechargeable battery: a perspective. *J. Am, Chem. Soc*. 135 (2013) 1167-76.

6. S.-W. Kim, D.-H. Seo, X. Ma, G. Ceder, K. Kang, Electrode Materials for Rechargeable Sodium-Ion Batteries: Potential Alternatives to Current Lithium-Ion Batteries. *Adv. Energy Mater*. 2 (2012) 710-721.

7. V. Palomares, P. Serras, I. Villaluenga, K.B. Hueso, J. Carretero-González, T. Rojo, Na-ion batteries, recent advances and present challenges to become low cost energy storage systems, *Energy Environ. Sci*. 5 (2012) 5884-5901.

8. H. Pan, Y.-S. Hu, L. Chen, Room-temperature stationary sodium-ion batteries for large-scale electric energy storage, *Energy Environ. Sci*. 6 (2013) 2338-2360.

9. G. Wang, L. Zhang, J. Zhang, A review of electrode materials for electrochemical supercapacitors, *Chem. Soc. Rev.* 41 (2012) 797-828.

10. V. Etacheri, R. Marom, R. Elazari, G. Salitra, D. Aurbach, Challenges in the development of advanced Li-ion batteries: a review, *Energy Environ. Sci*. 4 (2011) 3243-3262.

11. J. Liu, H. Xia, L. Lu, D. Xue, Anisotropic Co_3O_4 porous nanocapsules toward high-capacity Li-ion batteries, *J. Mater. Chem*. 20 (2010) 1506-1510.

12. B. Koo, H. Xiong, M.D. Slater, V.B. Prakapenka, M. Balasubramanian, P. Podsiadlo, C.S. Johnson, T. Rajh, E.V. Shevchenko, Hollow iron oxide nanoparticles for application in lithium ion batteries, *Nano Lett*. 12 (2012) 2429-2435.

13. X. Wang, X. Li, X. Sun, F. Li, Q. Liu, Q. Wang, D. He, Nanostructured NiO electrode for high rate Li-ion batteries, *J. Mater. Chem*. 21 (2011) 3571-3573.

14. M. Laurenti, N. Garino, S. Porro, M. Fontana, C. Gerbaldi, Zinc oxide nanostructures by chemical vapour deposition as anodes for Li-ion batteries, *J. Alloys Compd*. 640 (2015) 321-326.

15. M.-S. Park, Y.-M. Kang, G.-X. Wang, S.-X. Dou, H.-K. Liu, The Effect of Morphological Modification on the Electrochemical Properties of SnO_2 Nanomaterials, *Adv. Funct. Mater.* 18 (2008) 455-461.

16. S. Laruelle, S. Grugeon, P. Poizot, M. Dollé, L. Dupont, J-M. Tarascon, On the Origin of the Extra Electrochemical Capacity Displayed by MO/Li Cells at Low Potential, *J. Electrochem. Soc*. 149 (2002) A627-A634.

17. Y.-Y. Hu, Z. Liu, K.-W. Nam, O. J. Borkiewicz, J. Cheng, X. Hua, M. T. Dunstan, X. Yu, K. M. Wiaderek, L.-S. Du, K. W. Chapman, P. J. Chupas, X.-Q. Yang, C. P. Grey, Origin of additional capacities in metal oxide lithium-ion battery electrodes, *Nat. Mater*. 12 (2013) 1130–1136

18. W. Luo, X. Hu, Y. Sun, Y. Huang, Controlled synthesis of mesoporous MnO/C networks by microwave irradiation and their enhanced lithium-storage properties, *ACS Appl. Mater. Interfaces* 5 (2013) 1997-2003.

19. Y. Sun, X. Hu, W. Luo, F. Xia, Y. Huang, Reconstruction of Conformal Nanoscale MnO on Graphene as a High-Capacity and Long-Life Anode

Material for Lithium Ion Batteries, *Adv. Funct. Mater.* 23 (2013) 2436-2444.

20. M. Kundu, C.C. Ng, D.Y. Petrovykh, L. Liu, Nickel foam supported mesoporous MnO_2 nanosheet arrays with superior lithium storage performance, *Chem. Commun*. 49 (2013) 8459-8461.

21. X. Li, S. Xiong, J. Li, X. Liang, J. Wang, J. Bai, Y. Qian, MnO@carbon core-shell nanowires as stable high-performance anodes for lithium-ion batteries, *Chem. Eur. J.* 19 (2013) 11310-11319.

22. Z. Cai, L. Xu, M. Yan, C. Han, L. He, K.M. Hercule, C. Niu, Z. Yuan, W. Xu, L. Qu, K. Zhao, L. Mai, Manganese oxide/carbon yolk-shell nanorod anodes for high capacity lithium batteries, *Nano Lett*. 15 (2015) 738-744.

23. J.-G. Wang, C. Zhang, D. Jin, K. Xie, B. Wei, Synthesis of ultralong MnO/C coaxial nanowires as freestanding anodes for high-performance lithium ion batteries, *J. Mater. Chem. A*, 3 (2015) 13699-13705.

24. H. Jiang, Y. Hu, S. Guo, C. Yan, P.S. Lee, C. Li, Rational design of MnO/carbon nanopeapods with internal void space for high-rate and long-life li-ion batteries, *ACS Nano* 8 (2014) 6038-6046.

25. Y. Sun, X. Hu, W. Luo, Y. Huang, Porous carbon-modified MnO disks prepared by a microwave-polyol process and their superior lithium-ion storage properties, *J. Mater. Chem*. 22 (2012) 19190-19195.

26. Q. Hao, J. Wang, C. Xu, Facile preparation of Mn_3O_4 octahedra and their long-term cycle life as an anode material for Li-ion batteries, *J. Mater. Chem. A* 2 (2014) 87-93.

27. H. Li, P. Balaya, J. Maier, Li-Storage via Heterogeneous Reaction in Selected Binary Metal Fluorides and Oxides, *J. Electrochem. Soc*. 151 (2004) A1878-A1885.

28. Y.F. Zhukovskii, P. Balaya, E.A. Kotomin, J. Maier, Evidence for Interfacial-Storage Anomaly in Nanocomposites for Lithium Batteries from First-Principles Simulations, *Phys. Rev. Lett.* 96 (2006) 058302-058304.

29. Y. Deng, L. Wan, Y. Xie, X. Qin, G. Chen, Recent advances in Mn-based oxides as anode materials for lithium ion batteries, *RSC Adv*. 4 (2014) 23914-23935.

30. X. Liu, C. Chen, Y. Zhao, B. Jia, A Review on the Synthesis of Manganese Oxide Nanomaterials and Their Applications on Lithium-Ion Batteries, *J. Nanomater*. 2013 (2013) 1-7.

31. L. Mai, X. Tian, X. Xu, L. Chang, L. Xu, Nanowire electrodes for electrochemical energy storage devices, *Chem. Rev*, 114 (2014) 11828-11862.

32. Q. Li, L. Yin, Z. Li, X. Wang, Y. Qi, J. Ma, Copper doped hollow structured manganese oxide mesocrystals with controlled phase structure and morphology as anode materials for lithium ion battery with improved

electrochemical performance, *ACS Appl. Mater. Interfaces* 5 (2013) 10975-10984.

33. X. Wang, S. Qiu, G. Lu, C. He, J. Liu, L. Luan, W. Liu, Fabrication of porous MnO microspheres with carbon coating for lithium ion battery application, *CrystEngComm*. 16 (2014) 1802-1809.

34. Y. Zhang, Y. Yan, X. Wang, G. Li, D. Deng, L. Jiang, C. Shu, C. Wang, Facile synthesis of porous Mn_2O_3 nanoplates and their electrochemical behavior as anode materials for lithium ion batteries, *Chem. Eur. J*. 20 (2014) 6126-6130.

35. W. Zhao, N. Du, C. Xiao, H. Wu, H. Zhang, D. Yang, Large-scale synthesis of Ag–Si core–shell nanowall arrays as high-performance anode materials of Li-ion batteries, *J. Mater. Chem. A* 2 (2014) 13949-13954.

36. L. Groenendaal, F. Jonas, D. Freitag, H. Pielartzik, J. R. Reynolds, Poly(3,4-ethylenedioxythiophene) and Its Derivatives: Past, Present, and Future. *Adv. Mater*. 12 (2000**)** 481-494.

37. X. Wang, Y. Li, Selected-Control Hydrothermal Synthesis of α- and β-MnO_2 Single Crystal Nanowires, *J. Am. Chem. Soc*. 124 (2002) 2880-2881.

38. B. Ji, X. Jiao, N. Sui, Y. Duan, D. Chen, Long single-crystalline α-Mn_2O_3 nanowires: facile synthesis and catalytic properties, *CrystEngComm* 12 (2010) 3229-3234

39. T.T. Tung, T.Y. Kim, H.W. Lee, E. Kim, T.H. Lee, K.S. Suh, Conducting Nanocomposites Derived from Poly(styrenesulfonate)-Functionalized MWCNT-PSS and PEDOT, *J. Electrochem. Soc*. 156 (2009) K218-K222.

40. D. Chen, D. Chen, X. Jiao, Y. Zhao, Hollow-structured hematite particles derived from layered iron (hydro)oxyhydroxide-surfactant composites, *J. Mater. Chem*. 13 (2003) 2266–2270.

41. B. Gillot, M. E. Guendouzi, M. Laarj, Particle size effects on the oxidation-reduction behavior of Mn_3O_4 hausmannite, *Mater. Chem. Phys*. 70 (2001) 54-60.

42. P. A. Schultz, Shift in XPS levels in ionic adsorbate layers due to electrostatic effects, *Surf. Sci*. 209 (1989) 229-242.

43. K. Raj, J.A. Shanmugam, R. Mahalakshmi, R.B. Viswanathan, XPS and IR spectral studies on the structure of phosphate and sulphate modified titania - A combined DFT and experimental study, *Indian J. Chem. Sec. A* 49 (2010) 9-17.

44. D. Yonekura, E. Iwama, N. Ota, M. Muramatsu, M. Saito, Y. Orikasa, W. Naoi, K. Naoi, Progress of the conversion reaction of Mn_3O_4 particles as

a function of the depth of discharge, *Phys. Chem. Chem. Phys*. 16 (2014) 6027-6032.

45. P. Lu, C. Li, E.W. Schneider, S.J. Harris, Chemistry, Impedance, and Morphology Evolution in Solid Electrolyte Interphase Films during Formation in Lithium Ion Batteries, *J. Phys. Chem. C* 118 (2014) 896-903.

46. Z. Yang, Y. Feng, Z. Li, S. Sang, Y. Zhou, L. Zeng, An investigation of lithium intercalation into the carbon nanotubes by a.c. impedance, *J. Electroanal. Chem*. 580 (2005) 340-347.

47. Z. Chen, J.W.F. To, C. Wang, Z. Lu, N. Liu, A. Chortos, L. Pan, F. Wei, Y. Cui, Z. Bao, A Three-Dimensionally Interconnected Carbon Nanotube-Conducting Polymer Hydrogel Network for High-Performance Flexible Battery Electrodes, *Adv. Energy Mater*. 4 (2014) 1400207.

48. Y. Yao, N. Liu, M.T. McDowell, M. Pasta, Y. Cui, Improving the cycling stability of silicon nanowire anodes with conducting polymer coatings, *Energy & Environ Sci. 5* (2012) 7927-7930.

49. H. Xia, M. Lai, L. Lu, Nanoflaky MnO_2/carbon nanotube nanocomposites as anode materials for lithium-ion batteries, *J. Mater. Chem.* 20 (2010) 6896-6902.

50. M.A. Lowe, J. Gao, H.D. Abruña, In operando X-ray studies of the conversion reaction in Mn_3O_4 lithium battery anodes, *J. Mater. Chem. A* 1 (2013) 2094-2103.

51. L.-J. Her, J.-L. Hong, C.-C. Chang, Preparation and electrochemical characterizations of poly(3,4-dioxyethylenethiophene)/$LiCoO_2$ composite cathode in lithium-ion battery, J. Power Sources 157 (2006) 457-463.

52. C. Arbizzani1, M. Mastragostino, M. Rossi, Preparation and electrochemical characterization of a polymer $Li_{1.03}Mn_{1.97}O_4$/pEDOT composite electrode, Electrochem. Comm. 4 (2002) 545-549

53. X. Liu, H. Li, D. Li, M. Ishida, H. Zhou, PEDOT modified $LiNi_{1/3}Co_{1/3}Mn_{1/3}O_2$ with enhanced electrochemical performance for lithium ion batteries, J. Power Sources 243 (2013) 374-380.

54. L. Yue, S. Wang, X. Zhao, L. Zhang, Nano-silicon composites using poly(3,4- ethylenedioxythiophene):poly(styrenesulfonate) as elastic polymer matrix and carbon source for lithium-ion battery anode, J. Mater. Chem. 22 (2012) 1094-1099.

55. D.-L. Ma, Z.-Y. Cao, H.-G. Wang, X.-L. Huang, L.-M. Wang, X.-B. Zhang, Three-dimensionally ordered macroporous FeF_3 and its in situ homog-

enous polymerization coating for high energy and power density lithium ion batteries, Energy Environ. Sci. 5 (2012) 8538-8542.

6. Abstract (in Korean)

컨버젼 반응을 통해 리튬 이온을 저장하는 전이금속 산화물은 리튬 이온 배터리의 저장 물질로 널리 연구되고 있다. 하지만, 전이 금속은 충/방전 사이클을 거치면서 용량이 감소하는 데, 이러한 현상은 이 물질을 산업화 하는 데 걸림돌이 된다. 본 논문에서는 이러한 용량 감소를 해결하기 위해서, Mn_2O_3 나노와이어 물질에 전도성 고분자인 PEDOT:PSS (poly(3,4-ethylenedioxythiophene) polystyrene sulfonate)를 코팅하였다. 코팅된 PEDOT:PSS 는 표면의 저항을 감소시켰고, 충/방전 사이클을 거치면서 붕괴된 물질의 표면 사이에서 전자 경로를 제공하여 배터리 성능을 높였다.

α-Mn_2O_3/PEDOT:PSS 는 전류 밀도가 100 $mA \cdot g^{-1}$ 일 때, 200 사이클 이후에도 1450 $mAh \cdot g^{-1}$ 의 가역 용량을 보일 만큼 우수한 사이클 안정성을 보였다. 사이클에 다른 용량 증가는 다양한 산화수의 망간 산화물들과 망간 산화물 표면에서 생성된 겔과 같은 형태의 고분자의 가역적 반응에 의한 것으로 여겨진다. 이러한 결과는 PEDOT:PSS 가 전자

경로를 제공하고 충/방전 과정에 의해 생긴 물질의 붕괴를 막아주면서 전기화학적 활성을 증가 시킨 것을 설명해준다.

주요 핵심어 : 망간 산화물, PEDOT:PSS, 용량 증가, 컨버젼 반응, 리튬 저장 물질

Appendix

Fabrication of Three-Dimentionally Ordered Nickel Cobalt Sulfide Electrodes for Pseudocapacitor

1. Abstract

Three dimensionally ordered nickel cobalt sulfide electrode has been fabricated directly on stainless steel substrates as a current collector without binder or conducting agent. First, 350 nm silica nanoparticles dispersion is spin-coated on the stainless steel substrate to obtain three-dimensionally ordered silica template. And then SiO_2@nickel cobalt silicate core-shell structure was synthesized in aqueous solution of $Ni(NO_3)_2 \cdot 6H_2O$, $Co(NO_3)_2 \cdot 6H_2O$ and urea. The nickel cobalt silicate shell was converted into nickel cobalt sulfide through a hydrothermal reaction in the presence of Na_2S, where silica core are etched at the same time. The thickness of nickel cobalt silicate shell was changed by the concentration of nickel and cobalt precursor. Also, three-dimensional structure nickel cobalt sulfide was synthesized by proper quantity of sodium sulfide. The obtained nickel cobalt sulfide was characterized by Scanning Electron Microscopy (SEM), X-ray diffraction (XRD) and Electron dispersive spectroscopy (EDS).

2. Introduction

With the increase of the environment pollution, there are large development of field relating energy such as renewable energy, energy storage system (ESS), and so on. Besides, ESS is spotlighted because of development of electric vehicles (EVs). In recent, many researchers have been interested in electrochemical double layer capacitor (EDLC) or electrochemical supercapacitor (ES) due to high power density, long lifecycle, etc.

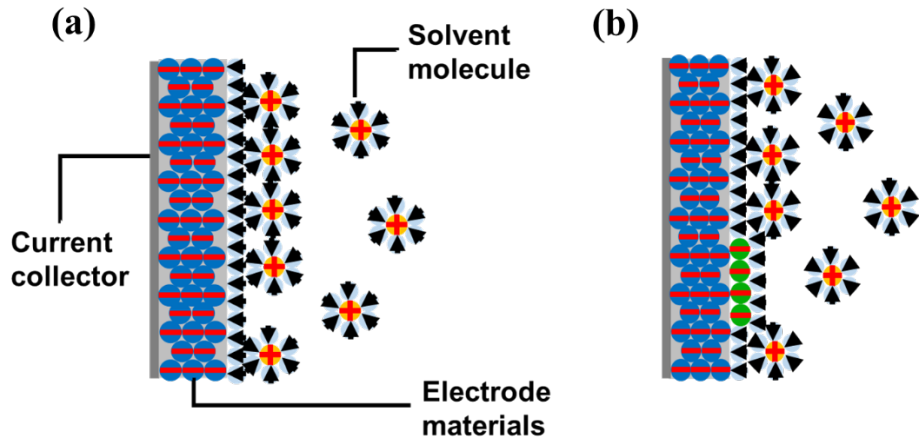

Figure A1. Principles of (a) EDLC (b) pseudocapacitor

There are two types of supercapacitor; **(1) EDLC** : Carbon based materials generally are used as electrode for EDLC. EDLC store energy in the electrolyte interfaces. Two electrolyte layer called “Helmholtz” double layer separate the charges between electrode materials and solvated opposite charged ions. The two opposite charged layer store the energy like conventional capacitor

and there is no charge transfer between electrode and adsorbed ion because they have only physical adsorption/desorption caused by electrostatic force not chemical bond. **(2) Pseudocapacitor** : unlike EDLC, pseudocapacitor stores electrical energy by reversible faradaic redox reaction. They have charge transfer between specific adsorbed ions and electrode materials. Transition metal oxides like RuO_2, IrO_2, and MnO_2 are used as electrode for pseudocapacitor. Normally, pseudocapacitor has larger capacitance than EDLC because they undergo faradaic redox reaction [1-3]. However, pseudocapacitor has poor structure and cycling stability comparing with EDLC because of the redox reaction of the electrode. Also, the poor conductivity of binder reduce performance, so many researchers challenge to fabricate binder-free supercapacitor electrode. For example, Huang et al. reported binder-free nickel based superpercapcitor electrode [4], and Lou et al. also made $NiCo_2O_4$ nanoneedle as binder-free supercapacitor electrode [5]. Especially, the three dimensional structure electrode attracted many interests as binder-free electrode [6]. Tang et al. and Liu et al. synthesized three-dimensionally ordered macroporous materials for supercapacitor [7-8]. In earliest pseudocapacitor research, RuO_2 is most actively studied but they are expensive and toxic. So, other transition metal oxides such as MnO_2, Ni_xO_y and Co_xO_y are rised as promising candidates for pseudocapacitor [1]. However the low intrinsic conductivity of metal oxide is still limitation as electrode for pseudocapacitor. To solve the problems things, doped-metal oxide or metal sulfide has been carried out recently due to their higher conductive characters [9-11]. Among

them, $NiCo_2S_4$ was attracted the researcher's interest because they have higher conductivity than other transition metal oxides and rich redox reaction [12-13]. And three-dimensionally structured materials have high surface area and effective ion diffusion path, so they have high rate capability, and excellent long-term cycle stability [14].

Here, we synthesized three-dimensional ordered structure $NiCo_2S_4$ and it did not use binder and any conductive agent. They have a tendency to vary thickness of shell by controlling amount of metal source. Furthermore, we found that the proper amount of sulfur source was needed for maintaining three-dimensional structure and the product has good potential to be material for supercapacitor.

3. Experimental section

Materials and Instruments

$Ni(NO_3)_2 \cdot 6H_2O$, $Co(NO_3)_2 \cdot 6H_2O$ and Na_2S purchased from Sigma-Aldrich. Tetraethyl orthosilicate (TEOS) purchased from TCI. And urea and NH_4OH purchased from Samchun Chemical Co. The morphologies of SiO_2, Ni-Co silicate and $NiCo_2S_4$ were confirmed by field emission scanning electron microscopy (FESEM, Hitachi S-4300). And the crystallographic phase of $NiCo_2S_4$ was identified by X-ray diffractometer (XRD, BRUKER MILLER Co., D8-Advance).

Synthesis of 350 nm SiO_2 nanoparticles

First, 10 mL of TEOS and 15 mL deionized water were mixed with 460 mL of 2-propanol. After 15 min stirring, 15 mL of NH_4OH was added dropwise and stirred overnight. Then, the white precipitation was washed with mixed solvent (H_2O : EtOH = 1 : 9, v/v) three times. And the precipitation was concentrated 800 mg/mL in the mixed solvent.

Spin coating on stainless steel (SUS) substrate

The circle stainless steel substrate with 1 cm diameter was attached with square glass. Then, the concentrated SiO_2 solution was dropped on the substrate and spun it 4,000 rpm for 1 min in spin coater. The coated substrates were annealed at 300 °C for 2 h due to more dense packing and better structure maintenance.

Synthesis of nickel cobalt silicate

The SiO_2 coated SUS substrate and 50 mg of urea were added in 5 mL of de-ionized water in glass vial. And nickel and cobalt mixture (Ni^{2+} : Co^{2+} = 1 : 2, n/n) was dissolved with three times weight of SiO_2 on substrate. Then, they were heated at 100 ºC for 12 h. After cooling, the substrate was washed with de-ionized water several times, and then nickel cobalt silicate on SUS substrate was obtained for next reaction.

Synthesis of nickel cobalt sulfide

The nickel cobalt silicate on SUS substrate was put in 5 mL of de-ionized water in Teflon-lined container. And Na_2S was dissolved 25 times more weight of nickel cobalt silicate on substrate. Then, they were reacted at 160 °C for 12 h in autoclave. The SUS substrate coated with dark-gray colored $NiCo_2S_4$ was washed with de-ionized water several times.

4. Result and Discussion

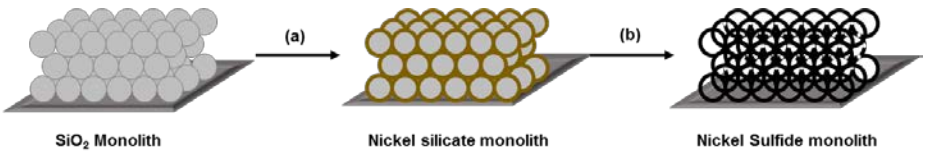

Scheme A1. Schematic illustrations of preparation of three-dimensionally ordered nickel cobalt sulfide. (a) Synthesis of nickel cobalt silicate shell on silica nanoparticles; (b) conversion to nickel cobalt sulfide with Na_2S.

In order to fabricate three-dimensionally ordered nickel cobalt sulfide directly on stainless steel substrate(SUS) as a current collector, first silica nanoparticles having diameters of 350 nm with a good size distribution were spin-coated on the SUS. And well-ordered template make more channel between particles and produce the stable electrodes. Therefore, the hexagonal packing was needed for ordered structure. The packing type was affected by viscosity and vapor pressure of solvent [15]. So, silica nanoparticles were dispersed in three types of solvent; (1) Type 1 (Only ethanol) (2) Type 2 (Butanol : ethylene glycol = 7 : 3, v/v), and (3) Type 3 (Ethanol : H_2O = 9 : 1, v/v). They showed different ordering trends by solvent type after spin coating.

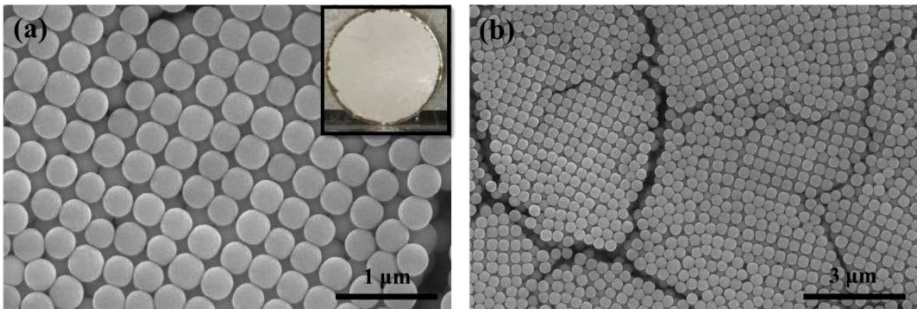

Figure A2. FE-SEM image of packing of SiO_2 nanoparticles in Type 1 (only ethanol) solvent. Inset is picture after spin coating.

SiO_2 nanoparticles formed cubic packing when they are in Type 1 solvent. Because ethanol solvent has low vapor pressure and ethanol was vaporized so fast, SiO_2 nanoparticles have no time to array hexagonal form. If SiO_2 nanoparticles have enough time to array, they would array hexagonal structure because the form is the most stable . But ethanol solvent had good affinity to SUS substrate, so SiO_2 nanoparticles were spin coated very well on SUS substrate.(Inset of **Fig. A2a**)

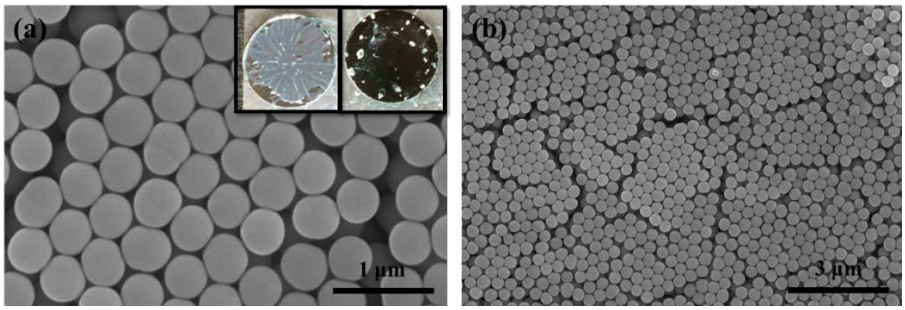

Figure A3. FE-SEM image of packing of SiO_2 nanoparticles in Type 2 (butanol : ethylene glycol = 7 : 3, v/v) solvent. Inset is picture after spin coating.

In Type 2 solvent, SiO_2 nanoparticles had hexagonal structure. Because butanol and ethylene glycol have low vapor pressure so they give enough time to array to SiO_2 nanoparticles. However, they also have high viscosity and poor adhesion with SUS substrate. As a result, SiO_2 nanoparticles were not spin coated well on SS substrate when they are in Type 2 solvent.(Inset of **Fig. A3a**)

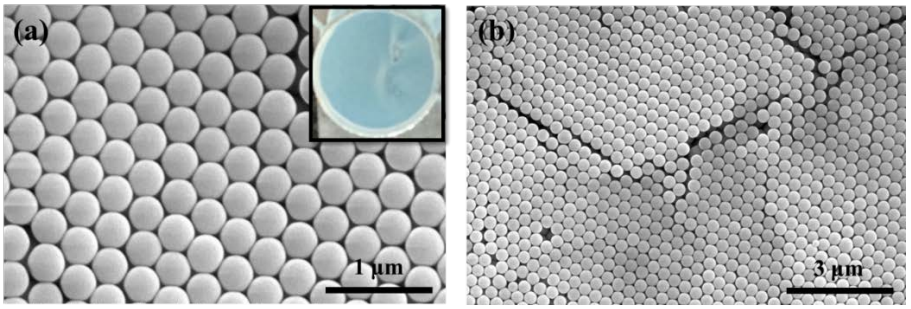

Figure A4. FE-SEM image of packing of SiO_2 nanoparticles in Type 3 (ethanol : H_2O = 9 : 1, v/v) solvent. Inset is picture after spin coating.

Considered packing and spin coating on substrate, proper vapor pressure, viscosity and adhesion with substrate are needed to make effective hexagonal ordered structure. When SiO_2 nanoparticles were dispersed in Type 3 solvent, they were spin coated very well and had perfect hexagonal packing. (**Fig.A4a**)

	Type I (Only EtOH)	Type II (BuOH : EG = 7:3)	Type III (EtOH : H_2O = 9:1)
packing	Cubic	Hexagonal	Hexagonal
Uniformity	O	X	O

Table A1. Packing and uniformity by solvent types.

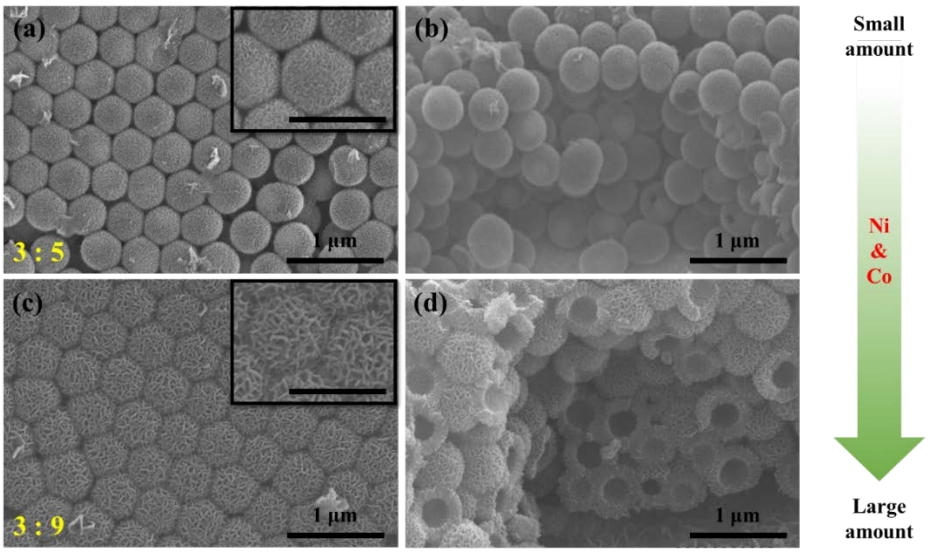

Figure A5. The morphologies of nickel cobalt silicate varying with nickel cobalt cation source. (a) FE-SEM top view (b) cross section view of nickel cobalt silicate when the ratio is 3 : 5 (SiO_2 : Ni/Co). (c) FE-SEM top view (d) cross section view of nickel cobalt silicate when the ratio is 3 : 9 (SiO_2 : Ni/Co). Scale bar of inset picture is 500 nm.

SiO_2 nano spheres were dissolved by urea to silicate anion, which produce nickel cobalt silicate through metal-ligand formation. SiO_2 nano spheres were activated by alkaline solution generated by the hydrolysis of urea [16-17]. Thickness nickel cobalt silicate shell was varied by the amount of nickel cobalt cation source. In Figure A5, the more the quantity of nickel and cobalt cation source, the thicker the nickel cobalt silicate shell.

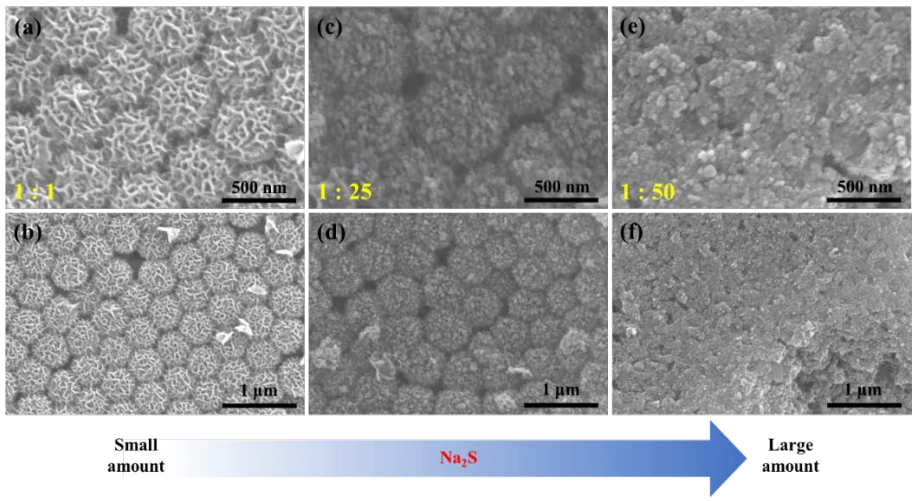

Figure A6. The trend of NCS varying with the amount of Na_2S. FE-SEM top view after reaction when the quantity of Na_2S is (a), (b) same (c), (d) 25 times (e), (f) 50 times.

In order to convert nickel cobalt silicate to nickel cobalt sulfide, SiO_2@nickel cobalt silicate was react with varying amount of Na_2S which serves as sulfurizing agent and silica template etching agent by generating basic environment [15]. When the amount of Na_2S is the same with nickel cobalt silicate, the sul-

fur substitution didn't happen because sulfur anion was running short to react sufficiently. Adding Na_2S with 25 times amount of nickel cobalt silicate, nickel cobalt sulfide were synthesized without structure decay. However, the structure was collapsed when the amount of Na_2S is 50 times. In water, Na_2S is decomposed to SH^- and OH^-; $Na_2S + H_2O \leftrightarrow 2Na^+ + SH^- + OH^-$ [15]. Therefore, excessive quantity of Na_2S made solvent too much basic and they etched SiO_2 core so fast before forming $NiCo_2S_4$ shell. (**Fig. A6**) The crystallinity of synthesized product was not good and they have $CoSO_4 \cdot 6H_2O$ because sulfur substitution was undergone in water. And the peak intensity of stainless steel is too high, so other peaks showed low intense, relatively. Although their crystallinity was not good, $NiCo_2S_4$ was well-synthesized. (**Fig. A7**)

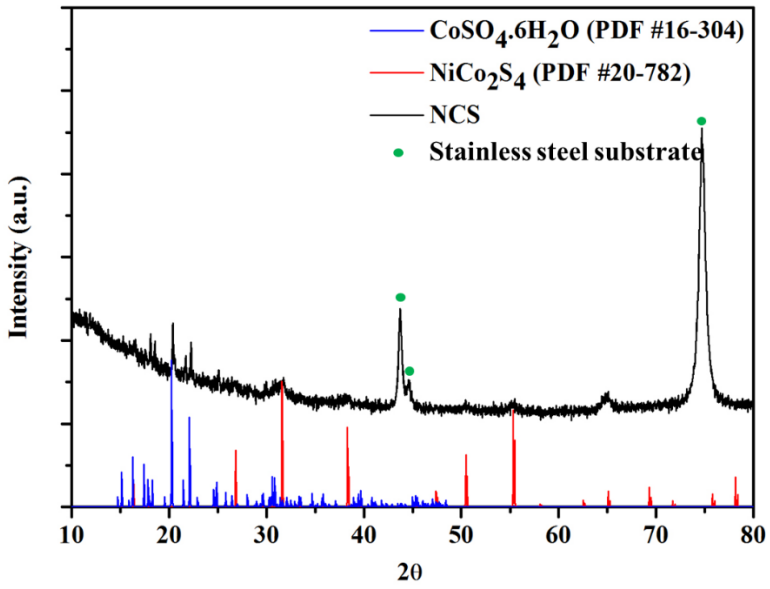

Figure A7. XRD patterns of synthesized NCS.

5. Conclusions

Three-dimensionally ordered nickel cobalt sulfide was successfully fabricated on stainless steel substrate for electrode of pseudocapacitor. Silica nano-spheres (nanoparticles?) were used as template for three-dimensionally ordered structures. The SiO_2 nanoparticles dispersions were spin-coated on stainless steel substrate and their packing morphology of nanoparticles was affected by the types of solvent that silica nano-spheres were arrayed hexagonal form in solvent consisting of water and ethanol. SiO_2@nickel cobalt silicate was obtained by reacting SiO_2 template with $Ni(NO_3)_2 \cdot 6H_2O$ and $Co(NO_3)_2 \cdot 6H_2O$. The thickness of nickel cobalt silicate increased with increasing the amount of metal ion sources. Nickel cobalt silicate were converted into nickel cobalt sulfide ($NiCo_2S_4$) in presence of Na_2S, and silica core was removed at the same time. Three-dimensional structure of $NiCo_2S_4$ was maintained by adjusting the amount of Na_2S. It is expected that this $NiCo_2S_4$ has high supercapacitive performance for pseudocapacitor.

6. References

1. G. Wang, L. Zhang, J. Zhang, A review of electrode materials for electrochemical supercapacitors, *Chem. Soc. Rev*., 41 (2012), 797-828

2. Y. Wang, Y. Xia, Recent progress in supercapacitor: From materials design to system construction, *Adv. Mater*., 25 (2013), 5336-5342

3. M. Winter, R. J. Brodd, What are batteries, fuel cells, and supercapacitors?, *Chem. Rev*., 104 (2004), 4245-4269

4. G. Zhang, W. Li, K. Xie, F. Yu, H. Huang, A one-step and binder-free method to fabricate hierarchical nickel-based supercapacitor electrodes with excellent performance, *Adv. Funct. Mater*, 23 (2013), 3675-3681

5. G. Q. Zhang, H. B. Wu, H. E. Hoster, M. B. Chan-Park, X. W. Lou, Single-crystalline $NiCo_2O_4$ nanoneedle arrays grown on conductive substrates as binder-free electrodes for high-performance supercapacitors, *Energy Environ. Sci*., 5 (2012), 9453-9456

6. Y. Li, L. Cao, M. Zhou, Y. Yang, P. Xiao, Y. Zhang, Ni-Co sulfide nanowires on nickel foam with ultrahigh capacitor for asymmetric

supercapacitors, *J. Mater. Chem. A*, 2 (2014), 6540-6548

7. W. Zhang, Y. Tan, Y. Gao, J. Wu, J. Hu, S. He, A. Stein, B. Tang, In_2O_3 nanoparticles on three-dimensionally ordered macroporous (3DOM) carbon for pseudocapacitor electrodes, *Electrochimica Acta*, 176 (2015), 861-867

8. Z. Liu, X. Tan, X. Gao, L. Song, Synthesis of three-dimensionally ordered macroporous manganese dioxide-carbon nanocomposites for supercapacitors, *Journal of Power Sources*, 267 (2014), 812-820

9. M. V. Reddy, G. V. Subba Rao, B. V. R. Chowdari, Metal oxides and oxysalts as anode materials for Li ion batteries, *Chem. Rev.*, 113 (2013), 5364-5457

10. J. Yang, X. Duan, Q. Qin, W. Zheng, Solvothermal synthesis of hierarchical flower-like ß-NiS with excellent electrochemical performance for supercapacitors, *J. Mater. Chem. A*, 1 (2013), 7880-7884

11. J. Xiao, L. Wan, S. Yang, F. Xiao, S. Wang, Design hierarchical electrodes with highly conductive $NiCo_2S_4$ nanotube arrays grown on carbon fiber paper for high-performance pseudocapacitors, *Nano Lett.*, 14 (2014), 831-838

12. H. Wan, J. Jiang, J. Yu, K. Xu, L. Miao, L. Zhang, H. Chen, Y. Ruan, $NiCo_2S_4$ porous nanotubes synthesis *via* sacrificial templates: high-performance electrode materials of supercapacitors, *CrystEngComm*., 15 (2013), 7649-7651

13. H. Chen, J. Jiang, L. Zhang, H. Wan, T. Qi, D. Xia, Highly conductive $NiCo_2S_4$ urchin-like nanostructures for high-rate pseudocapacitors, *Nanoscale*, 5 (2013), 8879-8883

14. M. J. Deng, P. J. Ho, C. Z. Song, S. A. Chen, J. F. Lee, J. M. Chen, K. T. Lu, Fabrication of Mn/Mn oxide core-shell electrodes with three-dimensionally ordered macroporous structures for high-capacitance supercapacitors, *Energy Environ. Sci*., 6 (2013), 2178-2185

15. A. Mihi, M. Ocaña, H. Míguez, Oriented colloidal-crystal thin films by spin-coating microspheres dispersed in volatile media, *Adv. Mater*., 18 (2006), 2244-2249

16. T. Zhu, Z. Wang, S. Ding, J. S. Chen, X. W. Lou, Hierarchical nickel sulfide hollow spheres for high performance supercapacitors, *RSC Adv*., 1 (2011), 397-400

17. J. Zheng, B. H. Wu, Z. Y. Jiang, Q. Kuang, X. L. Fang, Z. X. Xie, R. B. Huang, L. S. Zheng, General and facile synthesis of metal silicate

porous hollow nanostructures, *Chem. Asian. J.*, 5 (2010), 1439-1444